Clays Clay Miner. (2023) 71:513–538
https://doi.org/10.1007/s42860-023-00253-5

ORIGINAL PAPER

From Coupling Second-Order Stresses to Understanding and Predicting the Structural Response of a Dioctahedral Smectite

Chadha Mejri · Walid Oueslati · Abdesslem Ben Haj Amara

Accepted: 21 August 2023 / Published online: 13 October 2023

Abstract The employment of clay minerals in the transport of water, nutrients, and contaminants depends on a few factors, including permeability, hydration behavior, ion-exchange efficiency, and more. With the application of external stress, it is still difficult to understand how clay particles swell and collapse, how water is retained, how hydration heterogeneities are formed within crystallites, and how interlamellar space is organized. The present work studied the link between geochemical, thermal, kinetic constraints (established at the laboratory scale), and intrinsic clay features by exchanging Na-rich montmorillonite (SWy2) with Ni^{2+}, Mg^{2+}, or Zn^{2+} cations. By comparing the experimental 00*l* reflections with the calculated reflections obtained from the structural models, quantitative X-ray diffraction (XRD) analysis has enabled the building of a theoretical profile describing the layer stacking mode (LSM) and allowed the description of interlayer space (IS) configuration along the *c** axis. Regardless of the type of the exchangeable cations (EC), XRD modeling revealed that all samples exhibited interstratified hydration behavior within the crystallite size, which probably indicates partial or incomplete saturation of the IS. This theoretical result was defined by the appearance of two hydration states (1W and 2W), which were unrelated to the strain strength creating a higher degree of structural heterogeneity. Using the theoretical decomposition of the observed XRD patterns, the identification of all distinct layer populations and their stacking mode was achieved. The segregated LSM are, therefore, obviously superior as a function of stress strength.

Keywords Coupling Second-order Stresses · Geochemical, Thermal, and Kinetic Constraints · Montmorillonite · Quantitative XRD analysis

Associate Editor: Andrey G. Kalinichev

C. Mejri (✉) · W. Oueslati · A. Ben Haj Amara
Faculté des Sciences de Bizerte, LR19ES20, Ressources, Matériaux et Ecosystèmes (RME), Université de Carthage, 7021 Bizerte, Tunisie
e-mail: chadha.mejri@fsb.ucar.tn

Introduction

Montmorillonite (Mnt) belongs to the smectite (Sme) family; smectite is a 2:1 phyllosilicate (Kretz, 1983; Whitney & Evans, 2010; Warr, 2020). The Mnt structure is composed of a stack of two types of sheets: an octahedral sheet (MO_4 $(OH)_2$), represented by O, where M can be either Al or Mg, surrounded by two tetrahedral sheets (SiO_4), symbolized by T. This structure is known as T–O–T or 2:1, and has a layer thickness of ~9.6 Å (Brown, 1982; Drits & Tchoubar, 1990; Güven & Bailey, 1988; Moll, 2001; Newman, 1987). Additionally, there are isomorphic substitutions in the (T) and/or (O) sheets caused by the localization of cations of various natures in the various cavities. The Mnt is characterized by their large cation exchange

capacity (CEC), permeability, layered structure, various hydration properties, very large specific surface area (SSA), porosity, and resistance to mechanical stresses (Oueslati et al., 2022b). The CEC is an intrinsic feature of phyllosilicates and is defined by the compensating cations (CC) from the soil solution (SS) located in the interlamellar space (IS) (Bérend et al., 1995; Cases et al., 1997; Sato et al., 1992). The type of CC, amount and location of charge, as well as external factors such as thermal gradient, pressure, relative humidity (RH), and pH of the SS significantly affect this feature, which is the origin of the mineral hydration behavior. Indeed, the location of intrinsic layer charge and compensating cations, as well as the presence of water molecules in the interlamellar space (IS), determine the progressive expansion of the IS, known as the hydration process. This process causes the basal spacing of the 001 plane to vary discontinuously. Different hydration states (HS) can be defined based on the number of water layers intercalated in the IS: the dehydration state 0W (d_{001} ~ 10 Å), one-water hydration state 1W (d_{001} ~ 12.2 Å), two-water hydration state 2W (d_{001} ~ 15.4 Å), three-water layers 3W (d_{001} ~ 18.2 Å), and eventually four-water layers 4W (d_{001} ~ 21 Å). The type, amount, and location of compensating cations, as well as external factors such as thermal gradient, pressure, relative humidity (RH), and pH of the soil solution, affect significantly the hydration process, which is responsible for the mineral's hydration behavior (Bérend et al., 1995; Dazas et al., 2014, 2015; Oueslati & Meftah, 2018; Oueslati et al., 2011; Sato et al., 1992; Yan & Zhang, 2021). There are several other properties of clay minerals that are highly sensitive to changes in temperature gradients, kinetics during cation exchange processes, fluctuations in relative humidity, atmospheric pressure, the type and nature of CCs, as well as the solid–liquid ratio for heavy-metal removal (Ammar et al., 2014a, 2014b, 2014c; Berend, 1991; Coles & Yong, 2002; Es-Sahbany et al., 2019; Karmous et al., 2009; Marty et al., 2020; Meftah et al., 2010; Oueslati, 2019; Oueslati et al., 2006, 2012, 2017; Potgieter et al., 2006; Pufahl et al., 1983; Schroeder et al., 2004; Tournassat et al., 2013; Vidal et al., 2012; Yin & Zhu, 2016; Yuan et al., 2013).

The wide abundance of Mnt in nature and its low cost have made it suitable for various applications. It is known as one of the most effective materials for pollutant removal, especially in the field of mineralogy (Chaari et al., 2011; de Queiroga et al., 2019; Mahy et al., 2022; Nistor & Miron, 2007). Furthermore, it is utilized as a geological barrier for the containment of industrial and radioactive waste in deep disposal sites (Bobin et al., 2021). These sites are built on the multibarrier concept, which involves the combination of four interfaces: waste/metal package, metal package/concrete, concrete/clay, and clay/host rock (Abadie, 2020; Antoine et al., 2005; Dizier, 2011; Landrein, et al., 2013). These storage locations are situated typically at ~500 m below sea level. The main advantages of using geological clay liners in these sites are their large adsorption capacity for radioactive elements and their low permeability, which helps to slow down the migration of radionuclides in the host rock (Anastácio et al., 2008; Huber et al., 2015; Laverov et al., 2016; Pusch et al., 2012; Sellin & Leupin, 2013).

In the field of medicine, Mnt has shown promise as a drug-delivery system due to its large surface area and biocompatibility (Massaro et al., 2017; Mousavi et al., 2018; Neves et al., 2022; Panchal et al., 2018). In cosmetic compounds, Mnt has been used as a natural alternative to synthetic thickeners and emulsifiers (Whittaker et al., 2019). As an ion exchanger, Mnt can be used for the removal of heavy metals and other pollutants from wastewater (Carretero & Pozo, 2009, 2010; Gomes & Silva, 2007; Gubitosa et al., 2019; Hussain & Ali, 2021; Kang et al., 2019; Otunola & Ololade, 2020; Papadopoulos et al., 2014; Yingying et al., 2020).

Many studies have been conducted to investigate the adsorption properties of Mnt in various applications. The solid/liquid ratio is frequently a factor in the adsorption efficiency, as it affects the availability of active sites on the Mnt surface (Mejri et al., 2021). Overall, the unique properties of Mnt make it a valuable resource in many different fields. Usman et al. (2004) reported that a mere 4 to 8% of clay suspension can remove effectively up to 70% of heavy metals from a solution with an initial concentration of 100%. Furthermore, studies have shown that increasing the dose of the clay mineral results in an increase in adsorption (Wahba et al., 2017; Zhang et al., 2011).

While significant research has been conducted on the use of clay membranes for various applications, the impact of external stress coupling on clay membranes has not yet been addressed fully. Recent studies have shown that the binding selectivity of various

https://doi.org/10.1007/s42860-023-00253-5 Published online by Cambridge University Press

phases in a clay membrane can be affected by both chemical and mechanical stress activities (Whittaker et al., 2019). Additionally, clay membranes can change their structure in response to changes in pH and temperature (Meftah et al., 2011). In a recent study, Mejri et al., (2022a, 2022b) found that the exfoliation process and mesopore diameter of clay membranes increased with increasing strength of constraint coupling, including changes in SS pH and thermal gradient. The behavior of clay membranes in relation to hydration, porosity, selectivity, membrane permeability, CEC, adsorber performance, ion exchanger completion, and aging geomembranes can all be affected by constraint coupling (Ammar et al., 2014a, 2014b, 2014c; Bataillon et al., 2001). Furthermore, Marty et al. (2020) emphasized the relationship between the chemistry and hydration of clays and the preponderance of H_2O, considering the relative humidity and interstitial solution composition.

Many studies (Ammar et al., 2014a, 2014b, 2014c; Bataillon et al., 2001; Ishidera et al., 2022; Karmous et al., 2006; Oueslati et al., 2022b; Saravanan et al., 2015) have focused on the impact of individual parameters on clay material functionality, without taking into consideration the interplay of multiple environmental parameters that affect its behavior in real-world conditions.

A limited number of studies have employed this highly realistic methodology, as seen in works such as those by Chalghaf et al. (2013) and Whittaker et al. (2019). This methodology involves simulating real-world stresses at the laboratory scale using a well-defined scientific approach, including: (1) identifying the nature and intensity of the stresses applied to the mineral; (2) selecting the order of stress couplings to be performed; (3) implementing the chosen stress coupling in the laboratory; (4) characterizing the material's structural response; and (5) evaluating, optimizing, or explaining the results obtained.

The objective of the current study was to combine multiple physicochemical constraints at the laboratory scale to study the hydration behavior and structural response of Wyoming montmorillonite (W-Mnt) under the combined influence of geochemical, thermal, and kinetic perturbations. These constraints included variations in the pH of the SS saturated with different divalent cations such as Ni(II), Mg(II), or Zn(II), as well as modifications in temperature gradients and contact periods. The main goal of this study was to investigate the CEC and hydration behavior of the mineral, particularly the modifications in IS. The aim was to gain a comprehensive understanding of how these perturbations influence the mineral's response, specifically the changes in layer spacing configuration. To achieve this, a set of structural parameters was analyzed, including the type of compensating cation, the abundance of different layer types and their relative probability, the positioning of atoms/ions within the structure, the average number of layers ($\bar{N}$), layer stacking modes, and the quantity of water molecules. The quantification of mineral structure relied on the quantitative analysis of 00*l* reflections. This work is based on two main hypotheses. The first approach involved studying the impact of the dominance of a single applied constraint (zero order) while ignoring the coupling effects of the kinetic, thermal, and geochemical (second order) constraints on the mineral's structural response. The second hypothesis suggested that a direct relationship would be found among the properties of ionic potential (I_P), the electronegativity (E_N) of CC, and the migration of water molecules (H_2O) within the IS, resulting from changes in the d_{001} distance, thereby leading to the emergence of specific hydration behavior.

Materials and Methods

Baseline Material

Wyoming montmorillonite (W-Mnt), represented by SWy-2, is an American bentonite that served as the initial material. This Sme was obtained from the Source Clays Repository of The Clay Minerals Society (Moll, 2001). The W-Mnt is described by a half-cell structural formula, as follows (Mermut & Cano, 2001):

$$(Si^{4+}_{3.96}, Al^{3+}_{0.04})(Al^{3+}_{1.53}, Fe^{3+}_{0.18}, Fe^{2+}_{0.045}, Mg^{2+}_{0.26}, Ti^{4+}_{0.01})O_{10}(OH)_2(Ca^{2+}_{0.177}, K^{+}_{0.01}Na^{+}_{0.2}) \quad (1)$$

https://doi.org/10.1007/s42860-023-00253-5 Published online by Cambridge University Press

Pretreatment

To prepare a Na-rich montmorillonite suspension, a pretreatment of the starting material was performed. A small amount of clay (~10 g) was dispersed in a 1 M NaCl solution (~100 mL). The suspensions, named 'SWy-2,' underwent mechanical shaking for 24 h in the saline solution. Then, the solid fraction was separated by centrifugation, and fresh saline solution was added. This process was repeated four to five times to ensure the cation exchange process (CEP) was complete. Excess salt was removed by four to five washing cycles, each lasting 24 h, accompanied by sedimentation, supernatant removal, and immersion in deionized water. After the clay suspension (SWy-Na) was recovered, it was subjected to oven drying at 60°C for a period of 1 day. Following the drying process, it was removed from the oven.

Second-Order Coupling Constraints

Three metal cations (Ni^{2+}, Mg^{2+}, and Zn^{2+}) were studied and were selected mainly because of their common presence in industrial and radioactive waste, as well as their various properties (Ammar et al., 2018; Oueslati et al., 2009).

Second-order constraints were coupled by combining three external factors: geochemistry (variation of the pH of the soil solution), thermal gradients (variation of temperature, T in °C), and kinetics (variation of the duration of cationic exchange t in hours) at the laboratory scale.

To implement this approach, solutions of $NiCl_2$, $MgCl_2$, and $ZnCl_2$ (from MP Biomedicals, Illkirch-Graffenstaden, France) were prepared separately (250 mL, each sample) with a well defined pH (initially, pH = 2). The CEP was initiated by adding SWy-Na (0.5 g of powder for each solution). For each sample, a specific duration of mechanical agitation (initially set at $t = 5$ h) was applied concurrently with a specific temperature (initially set at 50°C). Afterward, a sample of the solution was taken and centrifuged at 4000 rpm (~×0.9 g) to separate the solid fraction from the liquid fraction. The solid fraction obtained was washed several times with distilled water to remove chloride ions (excess salt). The resulting samples were designated as SWy-M, where M represents a type of metal cation (e.g. SWy-Ni, SWy-Mg, and SWy-Zn).

For the solutions agitated for 5 h at pH = 2 and $T = 50$°C, an adjustment of the total volume of the MCl_2 solution was made to reach 250 mL by adding drops of hydrochloric acid or sodium hydroxide (HCl/NaOH) and distilled water, compensating for the volume decrease of the soil solution due to evaporation at 50°C (in the case of the first sample). The addition of NaOH was not random; it was done to increase the pH of the new solution by one pH unit (from 2 to 3). Then, a temperature increase was performed (in 25°C increments) by adjusting the T value on the magnetic-stirrer hot plate after each sampling, accompanied by a significant increase in the stirring duration (contact time of the sodic clay with the heavy metal), in steps of 5 h each time. This process was repeated multiple times until the final sample was obtained (pH = 6, $T = 150$°C, $t = 25$ h), (Fig. 1).

The three experiments were carried out simultaneously under the same atmospheric pressure, at the laboratory scale. The acidity and temperature of the solutions (MCl_2) were monitored using a pH meter and a thermometer, respectively. The duration of the cation exchange was measured using a stopwatch (Table 1).

To analyze the complexes obtained by X-ray diffraction, oriented samples were prepared by depositing the suspensions on glass slides in a dry environment for 24 h.

X-ray Diffraction (XRD)

To study crystal structures, a Bruker D8 ADVANCE X-Ray diffractometer (Bruker AXS GmbH, Karlsruhe, Germany) was used, equipped with CuKα monochromatic radiation (λ = 0.15406 nm) at 40 kV and 20 mA. The scan settings consisted of a step size of 0.01°2θ, a counting time of 6 s per step, and an angular range from 3.5 to 60°2θ. All experimental diffractograms were recorded at room temperature (Bizerte, Tunisia). The XRD research was carried out using a combination of semi-quantitative and quantitative analyses.

Semiquantitative and quantitative XRD analysis

The compounds studied were characterized and identified using XRD, as reported in previous studies (Leoni, 2008; Scardi & Leoni, 2002; Scardi et al.,

https://doi.org/10.1007/s42860-023-00253-5 Published online by Cambridge University Press

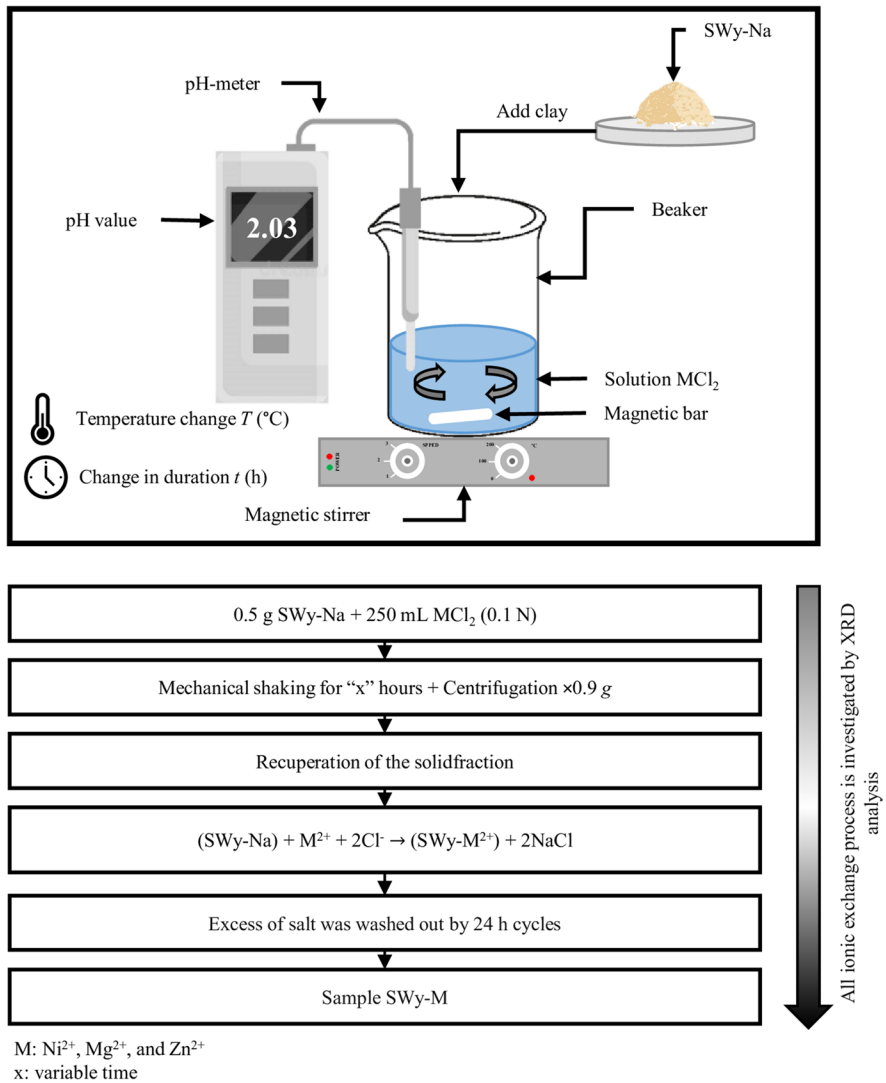

Fig. 1 Detail of the experimental protocol of the CEP under the effect of the second-order coupling of the applied constraints

Table 1 Experimental values of soil solution pH, temperature (*T*), and contact time (*t*) of the second-order constraint coupling applied

Coupling of the 2nd order				
Soil solution pH		Temperature (°C)	Time (h)	*V* (mL)
Acid	2	50	5	250
	3	75	10	
	4	100	15	
	5	125	20	
	6	150	25	

2011). Two associated analysis concepts were utilized to achieve this. The first was the 'semi-quantitative XRD analysis,' which involved determining the structure of the compounds by calculating the d_{001} basal intercalated value, the full width at half maximum (FWHM), the crystallite size (solved using the Scherrer equation), and the rationality parameter (ξ). The expression for ξ is as follows (Bailey, 1980; Ben Brahim et al., 1984):

$$\xi(\text{Å}) = \sum_{n=1}^{N} \left(\frac{d_{001} - 1 \text{ x } d_{001}}{n} \right) \quad (2)$$

https://doi.org/10.1007/s42860-023-00253-5 Published online by Cambridge University Press

The second was 'quantitative XRD analysis,' which involved determining the structural parameters (SP) at the nanoscale and provided a detailed overview of the interlamellar space (IS) contents, the arrangement of hydrated CC (M^{2+} + H_2O molecules), the average number of layers per stacking $\overline{M}$, the layer stacking mode (LSM), the homogeneity, and/or heterogeneity of the crystallites, crystallite defects, and more. This approach was implemented using an indirect modeling technique that involved comparing experimental profiles with theoretically predicted ones. This highlights the importance of conducting a quantitative investigation and the limitations of semiquantitative analysis in understanding the lamellar structure.

XRD profile modeling: Theoretical diffracted intensity and modeling strategy

Modeling diffractograms enables the quantification of mixed-layer structures (MLS) (Lanson, 2005), identification of the hydration state (0W → 3W), determination of structural heterogeneities, CEC variations, crystallite size D, optimal IS configuration, and average number of layers per crystallite. This indirect method follows a well determined mathematical formalism (Drits & Tchoubar, 1990), and the expression of the diffracted intensity for the space following the reciprocal z-axis is given by:

$$I_{00\downarrow}(^{\circ}2\theta) = L_p S_{pur} \mathrm{Re}[\phi][W]\left\{[I] + 2\sum_{n}^{\overline{M}-1}\left[\frac{\overline{M}-n}{n}\right][Q]^n\right\} \quad (3)$$

In the above equation, Re represents the real part of the final matrix, S_{pur} is the sum of the diagonal terms of the real matrix, L_p is the Lorentz polarization factor, $\overline{M}$ is the number of layers per stack, and n ranges from 1 to (1–$\overline{M}$–1). [Φ] is the matrix of structure factors, [I] is the identity matrix, [W] is the diagonal matrix of the proportions of the different types of layers, and [Q] is the matrix representing the interference phenomena between adjacent layers.

This indirect method allows for the determination of the abundance of different types of layers (W_i), the layer types of LSM, and the average number, $\overline{M}$, for the distributions of layers per coherent scattering domain (CSD) (Oueslati et al., 2012). Within a CSD, the stacking of layers is described by a set of junction probabilities (P_{ij}). The relationship between probabilities and the abundance W_i of two different layer types (i and j) can be described as follows: (1) segregation tendency is given by $W_i < P_{ii}$ and $W_j < P_{jj}$; (2) total demixing is obtained for $P_{ii} = P_{jj} = 1$; (3) regular tendency is obtained if $W_i < P_{ji} < 1$ and $W_j < P_{ij} < 1$; and (4) the boundary between the last distribution labeled chaotic or random is obtained when $Wi = P_{ji} = P_{ii}$, $W_j = P_{ij} = P_{jj}$ with $\Sigma W_i = 1$ and $\Sigma P_{ij} = 1$ (Drits & Tchoubar, 1990; Sakharov & Lanson, 2013).

The fitting strategy is an approach used to determine the structural parameters of materials from experimental XRD data (Oueslati et al., 2022a). It involves comparing the experimental diffractogram model with a theoretical model that is created using a principal interstratified structure. This theoretical model can be adjusted by introducing extra contributions, such as a mixed-layer structure, to account for any discrepancies between the experimental and theoretical models. The aim of this fitting process is to achieve an improved agreement between the theoretical and experimental models, which allows for the determination of the structural parameters of the material being studied.

The presence of two MLS does not imply that two particle populations exist physically in the sample (Ammar et al., 2014a, 2014b, 2014c; Ferrage et al., 2005a, 2005b; Lanson, 2005; Oueslati & Meftah, 2018). Therefore, layers with a similar HS appear in different MLS, contributing to the diffracted intensity, and are expected to have identical properties such as chemical composition, layer thickness, and z-coordinates of atoms. The XRD modeling method's details are explained extensively in previous work (Ammar et al., 2014a, 2014b, 2014c; Ferrage et al., 2005a, 2005b; Manohar et al., 2002; Oueslati & Meftah, 2018; Oueslati et al., 2012).

The z-coordinates in the T–O–T layer of the IS content (exchangeable cation, molecules, etc.) are optimized during the modeling process to reduce the disagreement between the theoretical and experimental findings (Table 2). This is controlled using an R_{WP} unweighted factor, expressed by Lanson (2011) and Laverov et al. (2016) as:

$$R_{WP} = \sqrt{\frac{\sum\left\{I(^{\circ}2\theta_i)_{exp} - I(^{\circ}2\theta_i)_{calc}\right\}^2}{\sum\left\{I(^{\circ}2\theta_i)_{exp}\right\}^2}} \times 100\% \quad (4)$$

To achieve optimal quantitative structural characterization of a given sample, it is necessary to search

https://doi.org/10.1007/s42860-023-00253-5 Published online by Cambridge University Press

Table 2 The types of atoms, their number, and their z-positioning along the *c** axis for the case of a TOT phyllosilicate

Atom type	O_1	O_2	O_3	O_4	O_5	O_6	OH_1	OH_2	Si_1	Si_2	Al
Number	2	1	2	2	1	2	1	1	2	2	2
Zn (Å)	0	0.20	2.25	4.31	6.26	6.59	1.98	4.28	0.59	6.04	3.43

for agreement between the calculated profiles and the experimental profiles (Bérend et al., 1995; Cases et al., 1997; Oueslati & Meftah, 2018), regardless of the type of hydration state of the layers or the position of the exchangeable metal cations (located in the middle of the IS along the *c** axis).

Modeling Strategy

Optimizing the structural parameters involves two steps. The first step is identifying the 'modulation function,' which is related to the positions of the characteristic XRD reflections. This is achieved by varying parameters such as the W_i proportions of different distances and P_{ij} relative probabilities of succession between different layer types (i and j), as well as the $\overline{M}$ average number of layers per stack. In the second step, adjustments are made to parameters such as the *z*-layer position atom composition along the *c** axis, the number and *z*-position of the exchangeable cations, and the abundance and configuration of interlayer water molecules, to improve the agreement between experimental and calculated profiles. The aim is to reduce the R_{WP} value to < 10%. The modeling strategy was summarized by Oueslati et al. (2022a), and previous studies have highlighted the importance of considering the abundance and configuration of interlayer water molecules in the optimization process (Ben Brahim et al., 1984; Ben Haj Amara, 1997; Oueslati et al., 2006; Sakharov & Drits, 1973; Sakharov & Lanson, 2013).

Results and Discussion

Semi-quantitative XRD Investigation of the Baseline Samples

The XRD experimental profile of the baseline SWy-Na (Fig. 2) of the reference (Mejri et al., 2022a, 2022b) exhibited the presence of three characteristic reflections ($n = 1$, 2, and 4). The first reflection ($n = 1$) was observed at a position of 7.16°2θ ($d_{001} = 12.33$ Å), suggesting the presence of a 1W HS (Table 3). The homogeneity of the observed character was verified by calculating the FWHM and ξ parameter value (Ferrage et al., 2007a, 2007b). The SWy-Na has been the subject of many studies as it was considered a reference sample (Ahmed et al., 2021; Altin et al., 1999a, 1999b; Alshabanat et al., 2013; Ammar et al., 2014a, 2014b, 2014c; Bérend et al., 1995; Cases et al., 1997; Chalghaf et al., 2012; Gregoire et al., 2020; Hu et al., 2017; Huber et al., 2015; Ishidera et al., 2022; Jiang et al., 2021; Karmous et al., 2006; Kozaki et al., 2010; Kraevsky et al., 2020; Lahbib et al., 2023; Leong et al., 2018; Liu & Yang, 2022; Liu et al., 2021; Mejri et al., 2023; Ohkubo et al., 2018; Oueslati & Meftah, 2018; Oueslati et al., 2012, 2015, 2022b; Saravanan et al., 2015; Sato et al., 1992; Scholtzová & Tunega, 2019; Segad et al., 2010; Shi et al., 2022; Tan et al., 2022; Tournassat et al., 2013, 2016; Wakou & Kalinichev, 2012; Wu et al., 2022; Yan & Zhang, 2021; Yotsuji et al., 2021; Zhang et al., 2018, 2022; Zhang et al., 2020; Zhu et al., 2022).

The nickel (SWy-Ni)- and magnesium (SWy-Mg)-saturated samples exhibited four characteristic reflections ($n = 1$, 2, 3, and 5) in their X-ray experimental patterns. The first reflections ($n = 1$) were located at ~ 6°2θ ($d_{001} \approx 14.7$ Å), indicating a mixed hydration state between 1 and 2W (Fig. 2). This suggested a heterogeneous (interstratified) character and an incomplete CEP (Table 3). These findings were consistent with previous research (Ammar et al., 2014a, 2014b, 2014c, 2018; Karmous et al., 2006; Oueslati et al., 2006).

In the zinc-saturated sample (SWy-Zn), an asymmetry was observed for the main 001 reflection, which was located at 7.18°2θ ($d_{001} \approx 12.3$ Å) due to the presence of sodium residue resulting from the starting sample SWy-Na (Fig. 2). Additionally, a shoulder toward the small angles around 5.9°2θ with $d_{001} \approx 15$ Å was observed, which was indicative of

https://doi.org/10.1007/s42860-023-00253-5 Published online by Cambridge University Press

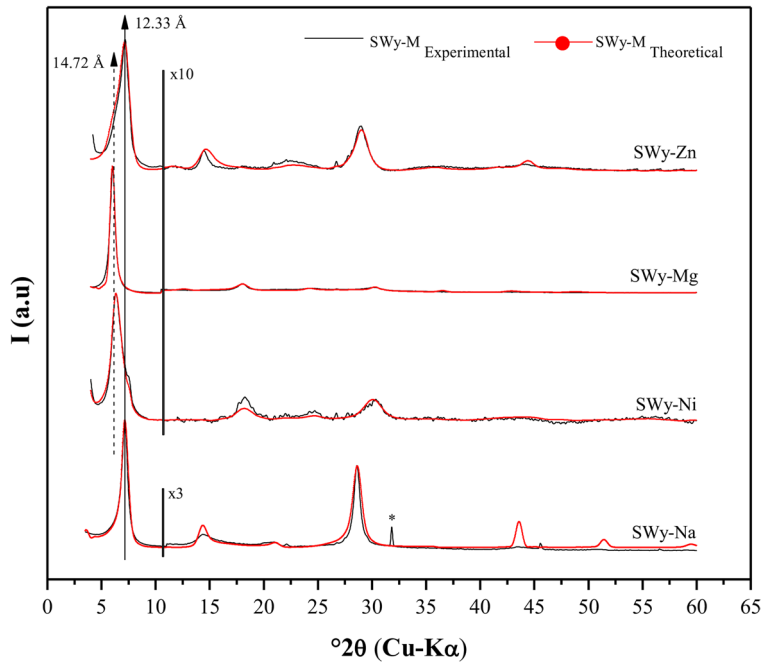

Fig. 2 Modeling of the experimental XRD patterns for the starting sample SWy-Na (Mejri et al., 2022) and the reference samples SWy-Ni, SWy-Mg, and SWy-Zn. (*) Halite, NaCl

a minor 2W HS presence allocated to the Zn^{2+} cation in IS (Jiang et al., 2021; Oueslati et al., 2009). In general, the perception of asymmetric 001 reflections indicated the appearance of a mixed HS in the crystallite and suggested a partial CEP.

(level2)Modeling of XRD Profiles of the Samples SWy-Na, SWy-Ni, SWy-Mg, and SWy-Zn.

Structural optimization using the X-ray modeling approach of the SWy-Ni, SWy-Mg, and SWy-Zn reference samples (Fig. 2) confirmed the heterogeneous character of the samples, with the presence of an MLS formed by 0W, 1W, and 2W, indicating an incomplete CEP (Lanson, 2005). The two hydration states, 0W and 1W, were attributed to the sodium residue from the starting sample SWy-Na. The IS was filled by the 'M' metal cation (Ni, Mg, and Zn) in the case of 2W.

According to bibliographic outcomes, only one water molecule sheet (H_2O) was detected in the middle of the IS along the c^* axis for the 1W phase, unlike the 2W phases where two water sheets enveloped the CC placed in the middle of the IS. The absence of H_2O in the IS was claimed for the dehydrated 0W phases (Ammar et al., 2014a, 2014b, 2014c; Bérend et al., 1995; Cases et al., 1997; Ferrage et al., 2005a, 2005b, 2010; Manohar et al., 2002; Oueslati et al., 2012; Sato et al., 1992). The average

Table 3 Qualitative X-ray analysis of the starting sample, SWy-Na (Mejri et al., 2022a, 2022b), and the reference samples SWy-Ni, SWy-Mg, and SWy-Zn

Sample	°2θ	d_{001} (Å)	FWHM (°2θ)	D (Å)	ξ (Å)	Character
SWy-Na (Mejri et al., 2022a, 2022b)	7.16	12.33	0.74	18.77	0.062	Homogeneous
SWy-Ni	6.30	14.02	1.27	10.93	0.670	Interstratified
SWy-Mg	6.03	14.65	0.55	25.24	0.120	
SWy-Zn	7.18	12.30	1.11	12.52	0.070	

°2θ Bragg's angle, d_{001} Basal distance of the 1st reflection, D average crystalline size, FWHM Full Width at Half Maximum, ξ Rationality deviation parameters

https://doi.org/10.1007/s42860-023-00253-5 Published online by Cambridge University Press

number of layers per crystallite was 10. Acceptable R_{WP} confidence factor values were obtained, reflecting the high quality of the fitting (Table 4).

Semi-quantitative Description of XRD Analysis after Applying Second-Order Coupling Stress

Case of the SWy-Ni samples

Based on the X-ray experimental results for the SWy-Ni samples, which were subjected to varying conditions of pH, temperature, and duration (pH = 2; T = 50°C; t = 5 h ⟶ pH = 4; T = 100°C; t = 15 h), an asymmetry was observed for the main 001 reflections at 5.8°2θ with $d_{001} \approx 15$ Å, indicating the presence of 2W, filled by Ni^{2+} cations in the middle of IS and bounded between two sheets of water. A shoulder toward the wide angles around 7°2θ ($d_{001} \approx 12.6$ Å) was also observed and was attributed to excess salt in the starting sample SWy-Na. The asymmetry of the 001 reflections was reflected in large values of FWHM and ξ, indicating the appearance of a set of hydration states in the mineral and an incomplete CEP. However, for samples with higher pH, temperature, and duration values (pH = 5; T = 125°C; t = 20 h / pH = 6; T = 150°C; t = 25 h), the absence of the shoulder toward the wide angles (linked to the sodium residue) was observed, and the symmetry of the 001 lines was probably due to a complete CEP (Table 5).

Case of the SWy-Mg samples

The X-ray experimental models for SWy-Mg samples obtained at low values of pH, T, and t (pH = 2; T = 50°C; t = 5 h ⟶ pH = 4; T = 100°C; t = 15 h) showed 001 reflections (n = 1) localized at ~5.9°2θ ($d_{001} \approx 14.9$ Å), indicating the appearance of two hydration states (1W and 2W) within the stacks accompanied by partial cation exchange (Ammar et al., 2018). The Mg^{2+} compensating cation could be distinguished from the starting sodium cation Na^{+} by XRD analysis at room conditions in this case (Table 5). For the other complexes (pH = 5; T = 125°C; t = 20 h / pH = 6; T = 150°C; t = 25 h), an increase in the FWHM value was observed, along with the creation of a stacking toward the wide angles (7.15°2θ ⟶ d_{001} = 12.35 Å), which was attributed to the sodium residue from the starting sample SWy-Na (Fig. 4).

Case of the SWy-Zn samples

The experimental X-ray diffractogram profiles of SWy-Zn samples (Fig. 5) revealed that, for most samples (pH = 2; T = 50°C; t = 5 h ⟶ pH = 5; T = 125°C; t = 20 h), the main 001-reflection was situated at ~5.8°2θ ($d_{001} \approx 15.2$ Å), indicating a 2W hydration state. This probably reflects a complete CEP (Oueslati et al., 2011). However, there was a slight deviation in the intensity of the 001-reflections

Table 4 Extraction of all structural parameters of the SWy-Na (Mejri et al., 2022a, 2022b), SWy-Ni, SWy-Mg, and SWy-Zn samples, via the modeling approach

Sample	%MLS	% 0W/1W/2W	L.Th 0W/1W/2W	nH_2O 0W/1W/2W	W_A	P_{AA}	R*	$\overline{M}$	C	% R_{WP}
SWy-Na (Mejri et al., 2022a, 2022b)	100	0W / 1W / ––	10.5 / 12.5 / ––	0 / 2 / ––	0.8	0.85	R_1	10	H	2.27
SWy-Ni	50	0W / 1W / ––	10.5 / 12.5 / ––	0 / 1 / ––	0.3	0.64	R_1	11	I	5.77
	50	–– / 1W / 2W	–– / 12.5 / 15.2	0 / 1.2 / 3.4						
SWy-Mg	20	0W / 1W / ––	10.5 / 12.5 / ––	0 / 1.2 / ––	0.2	0.22	R_1	12	I	4.28
	80	–– / –– / 2W	–– / –– / 15.2	–– / –– / 3.7						
SWy-Zn	80	0W / 1W / ––	10.5 / 12.5 / ––	0 / 2 / –	0.8	0.85	R_1	11	I	5.64
	20	–– / –– / 2W	–– / –– / 15.2	–– / –– / 4.2						

MLS Mixed Layer Structure, 0W/1W/2W Layer hydration state, L.Th Layer Thickness (Å), nH_2O Number of water molecules per half-cell, W_A Abundance of layer type A, P_{AA} Relative probabilities of succession law between two-layers type A, R* Reichweite factor R_0 and R_1 describe the MLS with random interstratifications or with partial segregation, respectively, $\overline{M}$ Average number of sheets per stack, C Character: H Homogeneous, I Interstratified, R_{WP} Confidence factor

https://doi.org/10.1007/s42860-023-00253-5 Published online by Cambridge University Press

Table 5 Qualitative X-ray analysis of the samples SWy-Ni, SWy-Mg, and SWy-Zn

Samples		°2θ	d_{001} (Å)	FWHM (°2θ)	D (Å)	ξ (Å)	Character
SWy-Ni	pH = 2; T = 50°C; t = 5 h	5.92	14.92	1.36	10.21	0.475	Interstratified
	pH = 3; T = 75°C; t = 10 h	5.88	15.02	1.30	10.68	0.364	Homogeneous
	pH = 4; T = 100°C; t = 15 h	5.84	15.12	1.04	13.35	0.217	
	pH = 5; T = 125°C; t = 20 h	5.76	15.33	0.83	16.73	0.232	
	pH = 6; T = 150°C; t = 25 h	5.72	15.44	0.95	14.61	0.188	
SWy-Mg	pH = 2; T = 50°C; t = 5 h	5.92	14.92	0.65	21.36	0.031	Interstratified
	pH = 3; T = 75°C; t = 10 h	5.91	14.94	0.68	20.42	0.040	
	pH = 4; T = 100°C; t = 15 h	6.14	14.38	0.70	19.84	0.377	
	pH = 5; T = 125°C; t = 20 h	5.91	14.94	0.97	14.31	0.267	
	pH = 6; T = 150°C; t = 25 h	5.95	14.84	1.16	11.97	0.427	
SWy-Zn	pH = 2; T = 50°C; t = 5 h	5.74	15.38	0.81	17.14	0.045	Homogeneous
	pH = 3; T = 75°C; t = 10 h	5.76	15.33	0.72	19.28	0.045	
	pH = 4; T = 100°C; t = 15 h	5.78	15.28	0.83	16.73	0.052	
	pH = 5; T = 125°C; t = 20 h	5.83	15.15	0.81	17.14	0.076	
	pH = 6; T = 150°C; t = 25 h	6.01	14.69	0.81	17.14	0.418	Interstratified

°2θ Bragg angle, d_{001} basal distance of the 1st reflection, D average crystalline size, FWHM full width at half maximum, ξ rationality deviation parameters

toward the wide angles with an increase in the applied coupling constraint intensity. The profile of the last sample (pH = 6; T = 150°C; t = 25 h) was positioned at ~ 6°2θ (d_{001} ≈ 14.7 Å), which was interpreted as the appearance of two hydration states (1W and 2W – interstratified structure), estimated by partial cation exchange, knowing that the zinc (Zn^{2+}) hydrate was bound to two layers of water 2W (~ 15 Å) (Table 5).

XRD Modeling Profiles after Applying Second-Order Coupling Stress

Case of the SWy-Ni samples

The quantitative XRD analysis of the SWy-Ni series indicated the appearance of two different hydration states as the amplitude of applied stresses increased (Fig. 3). The complexes with small values of pH, T, and t (pH = 2; T = 50°C; t = 5 h → pH = 4; T = 100°C; t = 15 h) indicated the emergence of two hydration states (i.e. 1W → d_{001} ≈ 12.2 Å and 2W → d_{001} ≈ 15.2 Å), with 2W being the dominant state. The CEC of the results obtained was satisfied partially by Na^+ and Ni^{2+} cations. This was because, under ambient conditions, sodium hydrated to form a single water layer (1W) (Oueslati & Meftah, 2018), while nickel hydrated with two water layers (2W). When the applied stress strength was increased, the interstratification spacing (IS) expanded, with the d_{001} value changing from 15 to 15.4 Å for samples with pH = 5, T = 125°C, and t = 20 h and pH = 6, T = 150°C, and t = 25 h. This expansion occurred due to the transition from an interstratified 1W/2W phase to a harmonically stacked 2W phase, which was saturated by Ni^{2+} cations only. The widening of the IS was attributed to the prolonged contact time (t ≈ 20 to 25 h) of the soil solution ($NiCl_2$) with the sample (Table 6).

Case of the SWy-Mg samples

Theoretical models obtained through modeling (Fig. 4) confirmed the heterogeneous character of the samples by establishing a correlation between two types of hydration phases, namely 1W/2W (intermediate phase), regardless of the intensity of the applied external stress. Specifically, the minor contribution of the 1W phase increased from 20 to 45% as the intensity of the applied external stress rose (pH = 2; T = 50°C; t = 5 h ⟶ pH = 6; T = 150°C; t = 25 h). This increase was attributed primarily to the presence of sodium residue in the SWy-Na starting sample. On the other hand, the major hydration state observed in the calculated profile was the 2W phase, which was associated with the layer fragment

https://doi.org/10.1007/s42860-023-00253-5 Published online by Cambridge University Press

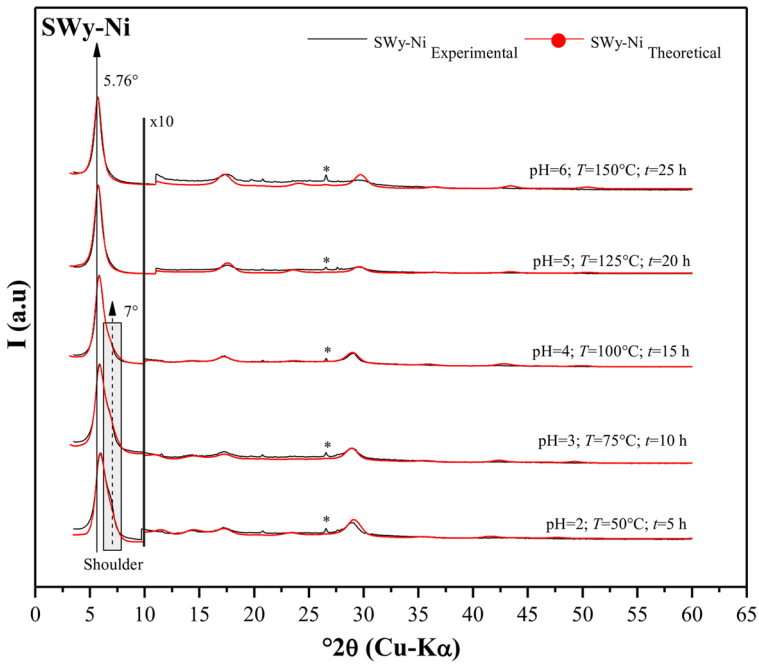

Fig. 3 Modeling of the experimental XRD patterns for SWy-Ni samples. (*) Halite, NaCl

saturated with the bivalent cation Mg^{2+}. This fluctuation in weighting suggests an incomplete (partial) CEP ($d_{001} \approx 14.8$ Å < 15 Å), which aligned with the qualitative analysis. Additionally, the slight shrinkage of the IS ($d_{001} \approx 14.92$ Å $\longrightarrow$ $d_{001} \approx 14.84$ Å) was due probably to the temperature increase during the CEP (Table 6).

Case of the SWy-Zn samples

The refinement of the experimental model (Fig. 5) uncovered the presence of two types of layers with a similar stacking mode (R_1), as determined by the modeling. This mixed-layer system (MLS) consists of two hydration states (Lanson, 2005), namely: (1) 1W with $d_{001} = 12.2$ Å, and (2) 2W with $d_{001} = 15.4$ Å. Throughout the entire series of experiments (ranging from pH = 2; $T = 50$°C; $t = 5$ h to pH = 6; $T = 150$°C; $t = 25$ h) a heterogeneous character was observed, characterized by a minor presence of the ubiquitous 1W HS (~20–35% abundance). This 1W state was saturated with the Na^+ cation, as reported by SWy-M (Oueslati & Meftah, 2018). Conversely, the major phase observed was the 2W phase (80–65% abundance), associated with the elemental part where the CEC was due probably to the temperature increase during the CEP (Table 6) saturated with the Zn^{2+} divalent cation (Tan et al., 2008; Oueslati et al., 2009; Shi et al., 2010). This indicated an incomplete CEP. During the CEP, the increase in temperature ($T \approx 50$°C $\longrightarrow$ 150°C) along with the variation in the pH of the SS (pH ≈ 2 $\longrightarrow$ 6) and the duration of contact (t ≈ 5 h $\longrightarrow$ 25 h) resulted in the closure (shrinkage) of the IS. This closure was evident from the decrease in the value of d_{001} (Table 6). It is important to note that, for all the samples examined in the current study, the Debye–Waller temperature factor (the mean square displacement of an atom from the ideal position in the structure) exhibited a variation ranging from 2.3 to 10.9 Å^2 (Ferrage et al., 2005a, 2005b, Ferrage, 2016).

In this study, the samples saturated with magnesium and zinc demonstrated similar hydration behavior under increasing imposed coupling constraint intensity, contrasting with the sample saturated with nickel. The interlayer space (IS) thickness decreased for SWy-Mg and SWy-Zn, resulting in a reduction of the 2W phase and an increase in the 1W phase. This indicated an incomplete cation exchange process (CEP). Conversely, for SWy-Ni, the IS thickness

https://doi.org/10.1007/s42860-023-00253-5 Published online by Cambridge University Press

Table 6 Extraction of all structural parameters of the SWy-Ni, SWy-Mg, and SWy-Zn samples, via the modeling approach

Samples		%MLS	xW-echa.cat	d_{001}	nH_2O	W_A	P_{AA}	R*	$\overline{M}$	$\overline{M}_{tot}$	C	R_{WP}
SWy-Ni	pH = 2; T = 50°C; t = 5 h	40	1W-Na	12.2	6.5	0.40	0.77	R_1	7	7	I	4.63
		60	2W-Ni	15.2								
	pH = 3; T = 75°C; t = 10 h	40	1W-Na	12.2	6.5	0.40	0.77	R_1	7	7	I	4.89
		60	2W-Ni	15.2								
	pH = 4; T = 100°C; t = 15 h	28	1W-Na	12.2	8.1	0.28	0.70	R_1	7	7	I	4.12
		72	2W-Ni	15.2								
	pH = 5; T = 125°C; t = 20 h	59	2W-Ni	15.2	8.4	1.00	1.00	R_0	7	6	H	6.03
		41	2W-Ni	15.2		1.00	1.00	R_0	4			
	pH = 6; T = 150°C; t = 25 h	53	2W-Ni	15.2	8.4	1.00	1.00	R_0	7	6	H	6.28
		47	2W-Ni	15.2		1.00	1.00	R_0	4			
SWy-Mg	pH = 2; T = 50°C; t = 5 h	20	1W-Na	12.2	5.9	0.20	0.00	R_1	9	9	I	5.39
		80	2W-Mg	15.4								
	pH = 3; T = 75°C; t = 10 h	25	1W-Na	12.2	6.3	0.25	0.30	R_1	10	10	I	5.74
		75	2W-Mg	15.4								
	pH = 4; T = 100°C; t = 15 h	40	1W-Na	12.2	6.8	0.40	0.25	R_1	10	10	I	8.12
		60	2W-Mg	15.4								
	pH = 5; T = 125°C; t = 20 h	40	1W-Na	12.2	7.3	0.40	0.60	R_1	10	10	I	5.18
		60	2W-Mg	15.4								
	pH = 6; T = 150°C; t = 25 h	45	1W-Na	12.2	7.3	0.45	0.69	R_1	10	10	I	5.57
		55	2W-Mg	15.4								
SWy-Zn	pH = 2; T = 50°C; t = 5 h	20	1W-Na	12.2	6.6	0.20	0.62	R_1	7	7	I	4.25
		80	2W-Zn	15.4								
	pH = 3; T = 75°C; t = 10 h	20	1W-Na	12.2	6.6	0.20	0.62	R_1	7	7	I	4.33
		80	2W-Zn	15.4								
	pH = 4; T = 100°C; t = 15 h	20	1W-Na	12.2	6.6	0.20	0.62	R_1	7	7	I	4.13
		80	2W-Zn	15.4								
	pH = 5; T = 125°C; t = 20 h	25	1W-Na	12.2	7.2	0.25	0.67	R_1	9	9	I	9.20
		75	2W-Zn	15.4								
	pH = 6; T = 150°C; t = 25 h	35	1W-Na	12.2	7.2	0.35	0.40	R_1	9	9	I	5.48
		65	2W-Zn	15.4								

MLS Mixed Layer Structure, xW-echa.cat Layer type and associated exchangeable cation, d_{001} interlamellar distance (Å); nH_2O number of water molecules per half-cell, W_A abundance of layer type A, P_{AA} relative probabilities of succession law between two-layers type A, R* Reichweite factor R_0 and R_1 describe the MLS with random interstratifications, or with partial segregation/order respectively, $\overline{M}$ average number of sheets per stack, $\overline{M}_{tot}$ total average number of sheets per stack, C Character: H Homogeneous, I Interstratified, R_{WP} Confidence factor

increased, suggesting a transition from an intermediate hydration state (1W/2W) to a homogeneous state (2W). This observation was confirmed by modeling and the absence and/or disappearance of the sodium residue.

In this work, two hypotheses were developed to explain the hydration behavior of the samples:

(1) The first hypothesis suggests that hydration behavior of the SWy-Mg and SWy-Zn series was primarily influenced by the remarkable increase in temperature, while the impact of modifying the pH value of the soil solution (SS), and the duration of contact can be ignored. Previous studies (Chalghaf et al., 2013; Cui et al., 2020; Meftah et al., 2010, 2011; Momeni et al., 2022; Tlemsani et al., 2022) demonstrated that the addition of an acidic and/or basic additive (HCl/NaOH) induced significant change in the mineral structure within a pH range of ~ 8–11 (basic medium). However, in the

https://doi.org/10.1007/s42860-023-00253-5 Published online by Cambridge University Press

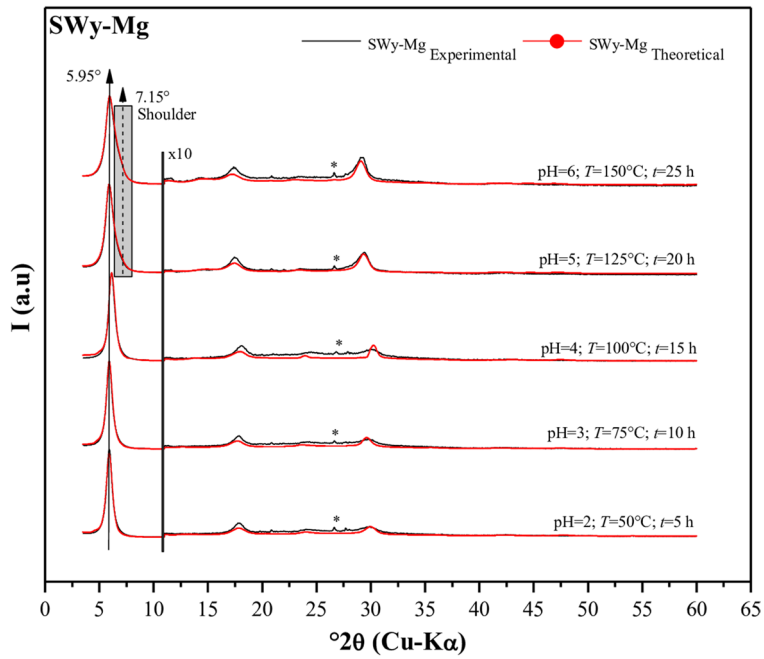

Fig. 4 Modeling of the experimental XRD patterns for SWy-Mg samples. (*) Halite, NaCl

present study, the pH of the SS varied from 2 to 6 and, thus, the impact of pH variation was considered negligible. Similarly, the duration of the CEP was also considered to be negligible. This conclusion was supported by the observation that, despite the relatively long contact time (~48 h) during

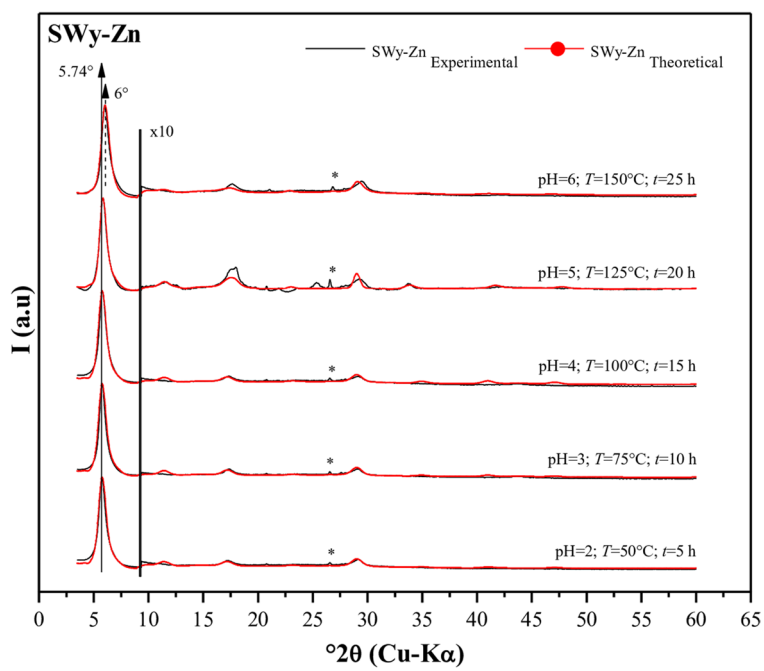

Fig. 5 Modeling of the experimental XRD patterns for SWy-Zn samples. (*) Halite, NaCl

https://doi.org/10.1007/s42860-023-00253-5 Published online by Cambridge University Press

the CEP, the d_{001} value of the reference sample SWy-Mg (Table 4) remained at ~14.65 Å, indicating partial cation exchange. The modeling further confirmed the presence of three hydration states 0W, 1W, and 2W with percentages of 6, 14, and 80%, respectively. This finding was consistent with the SWy-Mg sample (pH = 2; T = 50°C; t = 5 h) where the CEP lasted only 5 h (Tables 5 and 6) and resulted in an interlamellar distance of 14.9 Å, indicating incomplete cationic exchange. This condition was characterized by the appearance of two phases (1W ≈ 20% and 2W ≈ 80%). The similarity observed in these results challenges the assumption that the structure of the smectite (Sme) evolves with variations in the duration of the CE.

(2) The second hypothesis based on the present study considers the relationship between the ionic potential (I_P) and electronegativity (E_N) of different samples. SWy-Mg and SWy-Zn, which have the lowest I_P values of 2.78 and 2.70 eV, respectively (Shannon, 1976), display a similar hydration behavior (d_{001} ↘) as the imposed constraint strength increased. E_N also followed the same trend, with SWy-Mg having an E_N of 1.31 and SWy-Zn an E_N of 1.65 (Fig. 6). In contrast, for SWy-Ni, increasing the coupling constraint intensity resulted in the expansion of the interlayer spacing (IS) (d_{001} ↗), which was attributed to its high I_P value. For larger values, the I_P indicated a greater affinity of the cation for water, and as water migrates in the IS, the compensating cations M^{2+} also migrate, leading to IS swelling. It was noteworthy that the I_P value for Ni-saturated Mnt was 2.90 eV ($I_{P-SWy\text{-}Ni} > > I_{P-SWy\text{-}Mg} > I_{P-SWy\text{-}Zn}$), and E_N = 1.91 ($E_{N-SWy\text{-}Ni} > > E_{N-SWy\text{-}Zn} > E_{N-SWy\text{-}Mg}$). This hypothesis aligned with a similar study by Mejri et al., (2022a, 2022b), which investigated the influence of coupling first-order constraints (SS pH variation and thermal gradient) on three different metal cations (Co^{2+}, Cu^{2+}, and Ba^{2+}). The study demonstrated that Mnt samples saturated with compensating cations (SWy-Co and SWy-Cu) possessing larger I_P and E_N values ($I_{P-SWy\text{-}Co}$ = 3.08 eV > $I_{P-SWy\text{-}Cu}$ = 2.74 eV > > $I_{P-SWy\text{-}Ba}$ = 1.48 eV et $E_{N-SWy\text{-}Co}$ = 1.88 ≈ $E_{N-SWy\text{-}Cu}$ = 1.90 > > $E_{N-SWy\text{-}Ba}$ = 0.89) exhibited

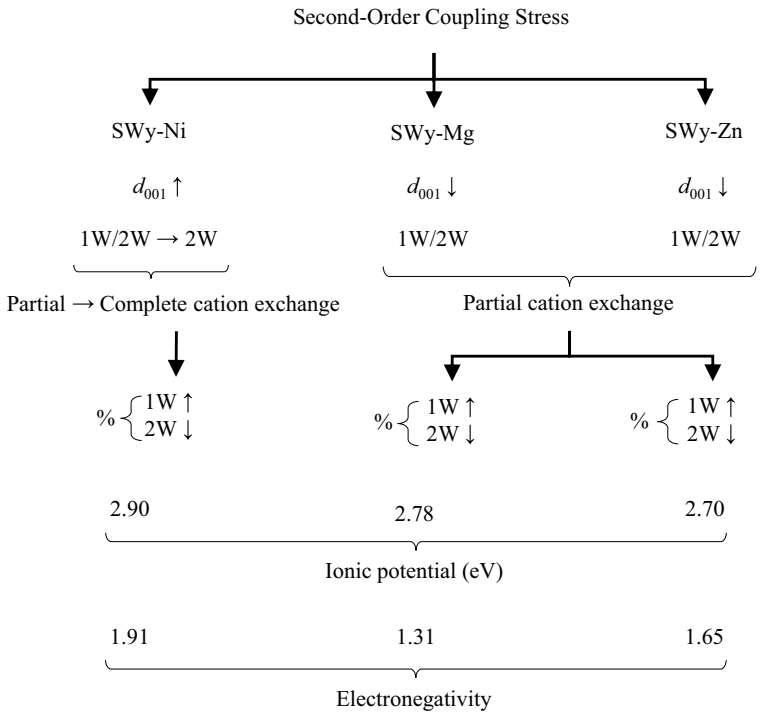

Fig. 6 Summary of the water behavior of SWy-Ni, SWy-Mg, and SWy-Zn samples under the effect of second-order coupling stress applied as a function of I_P and E_N, via an XRD modeling approach (Shannon, 1976)

https://doi.org/10.1007/s42860-023-00253-5 Published online by Cambridge University Press

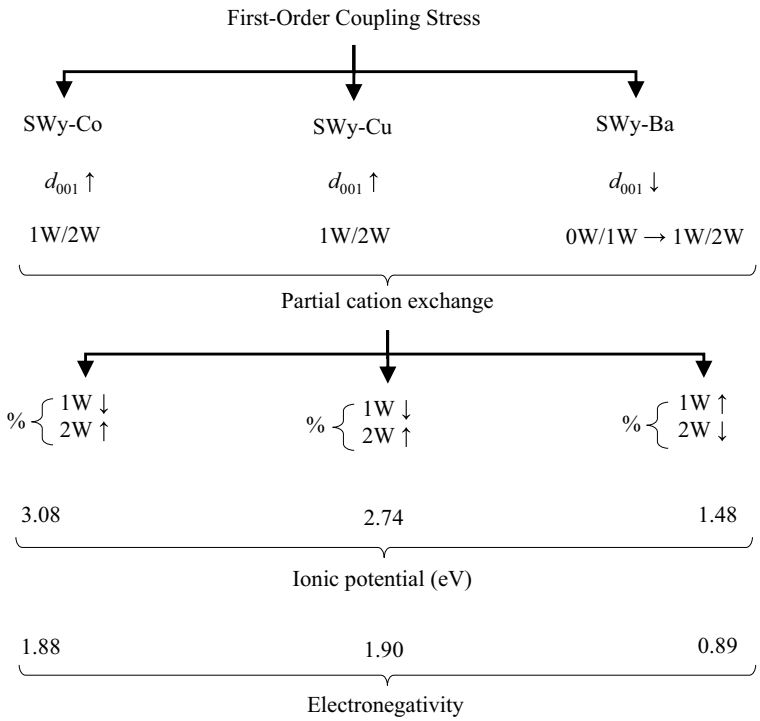

Fig. 7 Summary of the water behavior of SWy-Co, SWy-Cu, and SWy-Ba samples under the effect of first-order coupling stress applied as a function of I_P and E_N, via an XRD modeling approach (Mejri et al., 2022; Shannon, 1976)

a specific hydrous behavior, characterized by the expansion of IS (Fig. 7).

The increase in the percentage of the 2W phase was attributed to bivalent cations hydrating at two water layers. This leads to the development of an electronegativity limit (Fig. 8) that describes the hydrous behavior of Mnt saturated with metal cations (SWy-M) when subjected to similar external pressures with varying intensities.

The electronegativity limit defines the point at which layers of Mnt saturated with metal cations (SWy-M) start to open or close based on specific EN values (layer opening > 1.88 and layer closing < 1.65). An area of ambiguity exists between the values of 1.65 and 1.88 where the hydration behavior is not well understood. Therefore, additional experiments using different cations with varying I_P and E_N values should be conducted to gain further insight into this range of ambiguity.

Despite the originality of the first hypothesis, the rest of the work adopted the second idea because it seemed more logical.

It is important to note that the saturation of the monohydrated interlayers (1W) can occur not only with sodium (Na^+) but also with compensating cations such as Ni^{2+}, Mg^{2+}, or Zn^{2+}, depending on variations

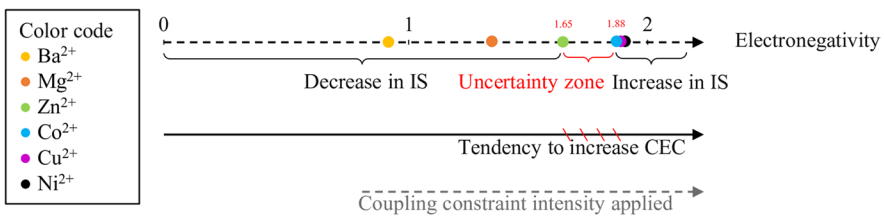

Fig. 8 Limit of the CEP as a function of the electronegativity of the compensating cations (Mejri et al., 2022; Shannon, 1976)

https://doi.org/10.1007/s42860-023-00253-5 Published online by Cambridge University Press

in the relative humidity levels (Ammar et al., 2014a, 2014b, 2014c; Ferrage et al., 2005a, 2005b; Oueslati et al., 2007, 2012). Because the RH was not taken into account during the acquisition of XRD data at the laboratory scale in this study, the 1W hydration phases were considered to be saturated exclusively with monovalent cations, while the 2W hydration phases were saturated exclusively with divalent cations. It is important to emphasize that these models are approximate, where everything is relative.

Evolution of the Water Molecule Abundances versus Coupling Constraint Strength

The variation in the amount of nH$_2$O affected directly the XRD profiles and influenced the higher-order 00l reflections (e.g. 002, 003, 004, 005, …) of the modeling approach (Oueslati et al., 2022a). The positioning and amount of H$_2$O depend on the hydration state (0W, 1W, 2W, 3W, and/or 4W), the type of CC (monovalent, divalent, trivalent, …) in the clay structure, as well as its position and charge (Babel & Kurniawan, 2003; Bérend et al., 1995; Bergaya & Lagaly, 2013; Cases et al., 1997; Ferrage, 2016; Ferrage et al., 2010; Komadel et al., 1996; Kozaki et al., 2010; Sato et al., 1992; Sun et al., 2015).

In the present case study, the coupling of the external second-order constraints resulted in fluctuations in the nH$_2$O value. The water affinity of the exchangeable cation (EC) was related directly to the ionic potential (I_P), which was defined by the ratio between the cation valence and its ionic radius (Shannon, 1976). An increase in I_P led to an increase in the water affinity of the cation. The compensating cations in this study (Ni^{2+}, Mg^{2+}, and Zn^{2+}) had high affinities ($I_{P—SWy\text{-}Ni} = 2.90$ eV $>> I_{P—SWy\text{-}Mg} = 2.78$ eV $> I_{P—SWy\text{-}Zn} = 2.70$ eV), r esulting in an homogeneous 2W HS and two heterogeneous 1W/2W states, respectively (Bérend et al., 1995; Cases et al., 1997). In contrast, monovalent cations (i.e. Na^+ and Cs^+) have low water affinity, which was reflected by a 1W HS state. Quantitative analysis using XRD showed a slight increase in the amount of nH$_2$O per half-unit cell (Fig. 9) as a function of the increase in the applied constraints (second-order coupling constraint) for the three series (SWy-Ni, SWy-Mg, and SWy-Zn). These results were predictable, following the increase in

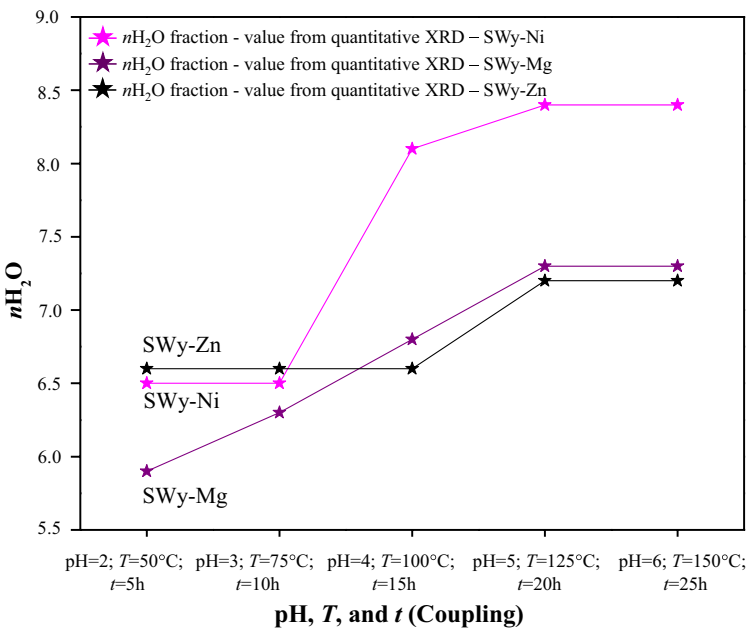

Fig. 9 The evolution of the abundance of the nH$_2$O as a function of the intensity of the external constraints applied for the SWy-Ni, SWy-Mg, and SWy-Zn series

https://doi.org/10.1007/s42860-023-00253-5 Published online by Cambridge University Press

temperature, which was automatically affected by the CEC and the IS closure.

Evolution of the 1W and 2W Abundances versus Constraint Strength

The graph in Fig. 10 was labeled as the 'water footprint' (WF) for the three series, illustrating the combination of two + hydration states (1W and 2W) within the particle. The completeness or incompleteness of the CEP can be influenced by the change in the d_{001} value (Oueslati & Meftah, 2018). The hydration behavior of the SWy-Ni series showed a decrease in the 1W monohydrate state (from 40 to 0%), and by an increase in the fluctuation for the 2W hydration state (from 60 to 100%). This was interpreted as easy intercalation of the CC (Ni^{2+}) in the IS, gradually replacing the sodium cations (Na^{+}) and causing their removal from the structure. This effect became more pronounced with an increase in the applied stress intensity, as seen in extreme cases such as pH = 5, T = 125°C, and t = 20 h and pH = 6, T = 150°C, and t = 25 h. This supports the completion of the CEP, despite the presence of the established stress coupling.

The SWy-Mg and SWy-Zn series exhibited different water behavior from the SWy-Ni series. A slight increase in the 1W HS was followed by a gradual decrease in 2W HS, with a significant domination of 2W HS. This decrease in the IS reflected a partial cation exchange that occurred as applied stresses intensified, even though there was an equilibrium time provided for the exchange.

The analysis of the optimized theoretical mixed-layer systems (MLS) used to replicate the experimental X-ray models revealed that the 2W HS was the most abundant phase in the three complexes (SWy-Ni, SWy-Mg, and SWy-Zn), in contrast to the 1W HS. This observation indicates that the 2W phase was the dominant phase in these systems (Fig. 10).

Evolution of the Average Number of Layers

The manipulation of the average number of layers ($\overline{M}$) was a critical factor in examining the clay's response and analyzing the crystal structure (Fig. 11) through XRD analysis for the three series (SWy-Ni, SWy-Mg, and SWy-Zn). The variation in $\overline{M}$ directly influenced the characteristics of the primary 001 observed in both the experimental and calculated models. Specifically, larger values of $\overline{M}$ (~ 10) resulted in narrow 001-peaks with smaller FMWH values, while smaller values of $\overline{M}$ led to broader 001 peaks with larger FMWH values (Oueslati et al., 2022a).

Evolution of the Layer Stacking Mode (LSM)

XRD modeling patterns were employed to characterize the hydration states associated with each optimal configuration derived from the best agreements achieved between the calculated and experimental XRD models of the three series SWy-Ni, SWy-Mg, and SWy-Zn (Table 7). The overall appearance of the LSM exhibited partial segregation. A more detailed analysis revealed specific stacking modes for each series. The SWy-Ni series exhibited a combination of two stacking modes – partial and total segregation. In the case of the SWy-Mg series, two stacking modes were observed – partial order and total segregation. Finally, for the SWy-Zn series, a single stacking mode (partial segregation) was observed.

Summary and Conclusions

The present study investigated the impact of coupled geochemical, thermal, and kinetic factors on the hydration behavior and structural response of W-Mnt. The research aimed to understand the effectiveness of CEC and the reversibility, hydration properties, and resistance of Na-rich montmorillonite exchanged with divalent metal cations M^{2+} (Ni^{2+}, Mg^{2+}, or Zn^{2+}) under the application of second-order external constraints. The objectives of the study were achieved by subjecting the mineral to stress at the laboratory scale, which entailed coupling three constraints simultaneously: geochemical, thermal, and kinetics. This was possible by varying the pH of the depolluting solution under controlled temperatures for various durations. The mineral's CEC and hydration behavior were the main areas of investigation, and the research relied on the quantitative analysis of the 00l reflections to quantify the structure of the mineral. The results showed that the external constraints applied to the samples had a significant impact on the mineral's response. The study found that the electronegativity of the compensating cation was associated with a limit that governed

https://doi.org/10.1007/s42860-023-00253-5 Published online by Cambridge University Press

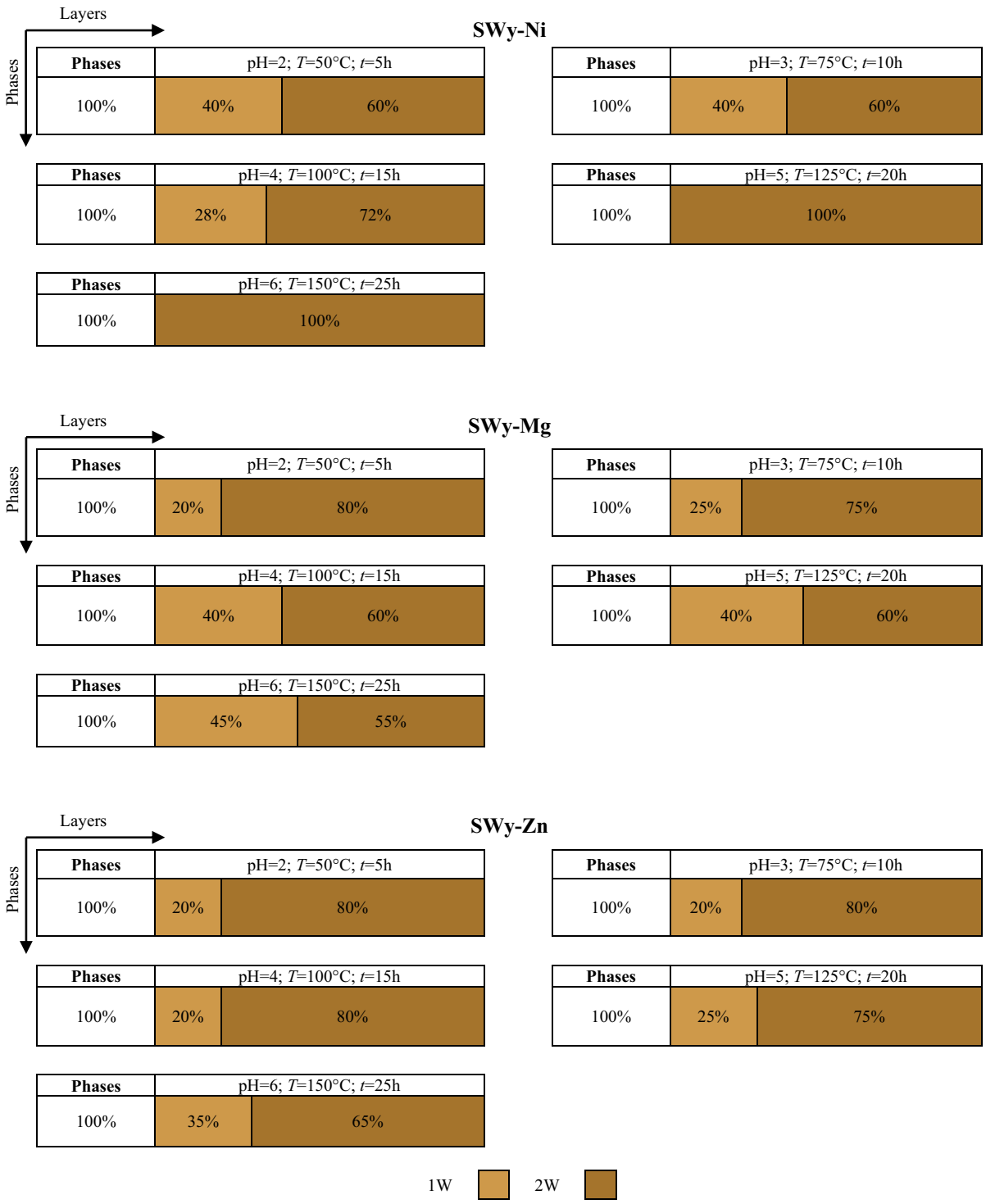

Fig. 10 Graphical representation of weighting of hydration states (1W and 2W) obtained via a modeling approach of the XRD patterns for the SWy-Ni, SWy-Mg, and SWy-Zn series (color code: 1W - light brown and 2W - dark brown)

https://doi.org/10.1007/s42860-023-00253-5 Published online by Cambridge University Press

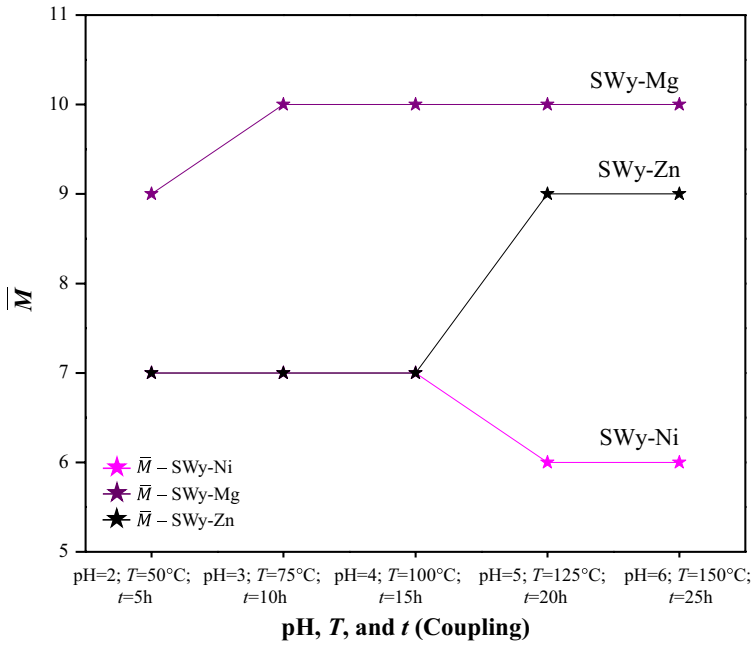

Fig. 11 Evolution of the $\overline{M}$ value as a function of the intensity of the external constraint applied for the SWy-Ni, SWy-Mg, and SWy-Zn series

the increase or decrease of the CEC. Each sample had a unique structural feature and responded differently to changes in the applied constraints over time. To ascertain the relationship between the applied external stresses and the structural evolution/alteration of the host materials, the XRD profile modeling approach was used, which uses numerous skills in simulating 00*l* reflections and improving agreement between calculated and experimental diffracted intensities to reveal clay surface reactivity and crystallography of lamellar structures.

Table 7 Stacking modes hydration layers for the SWy-Ni, SWy-Mg, and SWy-Zn series

Samples		Layer stacking mode R*	Description
SWy-Ni	pH = 2; T = 50°C; t = 5 h	R_1	Partial segregation
	pH = 3; T = 75°C; t = 10 h	R_1	Partial segregation
	pH = 4; T = 100°C; t = 15 h	R_1	Partial segregation
	pH = 5; T = 125°C; t = 20 h	R_0	Total segregation
	pH = 6; T = 150°C; t = 25 h	R_0	Total segregation
SWy-Mg	pH = 2; T = 50°C; t = 5 h	R_1	Partial order
	pH = 3; T = 75°C; t = 10 h	R_1	Partial segregation
	pH = 4; T = 100°C; t = 15 h	R_1	Partial order
	pH = 5; T = 125°C; t = 20 h	R_1	Partial segregation
	pH = 6; T = 150°C; t = 25 h	R_1	Partial segregation
SWy-Zn	pH = 2; T = 50°C; t = 5 h	R_1	Partial segregation
	pH = 3; T = 75°C; t = 10 h	R_1	Partial segregation
	pH = 4; T = 100°C; t = 15 h	R_1	Partial segregation
	pH = 5; T = 125°C; t = 20 h	R_1	Partial segregation
	pH = 6; T = 150°C; t = 25 h	R_1	Partial segregation

https://doi.org/10.1007/s42860-023-00253-5 Published online by Cambridge University Press

In detail, the integration of theoretical findings obtained through XRD modeling with experimental patterns showed that, at room temperature, the initial SWy-Na sample exhibited an interstratified hydration state of the 0W and 1W phases. For the reference samples SWy-Ni, SWy-Mg, and SWy-Zn, which were analyzed without any applied constraint, the XRD analysis indicated the presence of three phases, namely 0W, 1W, and 2W. The semi-quantitative XRD analyses of the results obtained under the impact of the second-order coupling were as outlined below.

Several observations were made in relation to the impact of second-order coupling in the SWy-Ni series, as follows. (1) A greater intensity of applied stress induced a transition from a heterogeneous hydration state (HS) characterized by the presence of 1W and 2W phases to a homogeneous HS where only a single type of 2W layer population existed. This transition coincided with the elimination of sodium residues. (2) Two distinct stacking modes for the layers were identified in the theoretical XRD patterns. (3) Throughout the entire series, the dominant stacking mode was referred to as 'total segregation.' (4) The CEC increased simultaneously with the increase in applied constraint intensity. (5) The number of water molecules ($n$$H_2O$) increased non-linearly in response to the development of applied constraints. (6) Irrespective of the applied stresses, an independent increase in the average number of layers ($\overline{M}$) occurred.

The SWy-Mg series yielded several noteworthy findings. (1) A heterogeneous hydration state was observed, with the appearance of both 1W and 2W phases regardless of the applied stress. (2) The intensification of external stress led to a decrease in the 2W phase and an augmentation of the 1W phase. (3) Diverse layer types coexisted within the crystallite and exhibited stacking patterns guided by specific junction probabilities, characterized by partial order and segregation. (4) The applied stress caused a reduction in the CEC, and the presence of two distinct compensating cations (Na^+ and Mg^{2+}) indicated partial cation exchange, independent of the applied stress. (5) A non-linear growth in the amount of H_2O was observed as the external stresses increased.

In the SWy-Zn series, several notable observations were made. (1) The coexistence of multiple populations of layer types (1W and 2W) confirmed the presence of an interstratified hydration character, unaffected by the applied stress. (2) The dominance of the 2W HS was particularly pronounced. (3) The CEP remained incomplete, independent of the external constraints exerted. (4) The presence of two distinct compensating cations (Na^+ and Zn^{2+}) within the IS resulted in the formation of a physical mixture between populations of different layer types. (5) Throughout the entire series, a single stacking mode characterized by partial segregation was observed. (6) The amount of H_2O exhibited a nonlinear increase in response to the applied external stresses. (7) The expansion of the IS led to an increase in the $\overline{M}$ values for both SWy-Mg and SWy-Zn samples, irrespective of the magnitude of the applied stress. In fact, the electronegativity of the compensating cation (CC) was associated with a limit that governs the increase or decrease in the CEC. Samples saturated with EC and E_N values > 1.88 show a rise in CEC, while samples saturated with cations with an EN value of ≤ 1.6 exhibit a drop in CEC. The hydration performance for E_N values between 1.65 and 1.88 (the uncertainty zone) was considered unidentified. The optimization of the modeling approach enabled the mapping of interstratified hydration layers and the development of the WF concept. Each sample has a unique structural feature and responds differently to changes in the applied constraints over time.

In conclusion, our thorough investigation of smectites sheds important light on how they react to geochemical, thermal, and kinetic limitations. The findings demonstrate the importance of the ionic composition, particularly the electronegativity of exchangeable cations, in determining the characteristics of clays. The CEC fluctuates according to the constraints strength, and it appears that higher electronegativity compensatory cations are required to reach a greater CEC. Furthermore, the observed variations in crystalline configurations, ranging from complete segregation to the partial order, show how susceptible clay formations are to external stresses. An accurate depiction of the intricate hydration states of smectite is made possible by the unconventional approach involving the use of a clay hydration background data. These results highlight the critical role played by a combination of external environmental limits in the prediction and control of smectite specific features. These

https://doi.org/10.1007/s42860-023-00253-5 Published online by Cambridge University Press

findings have important ramifications for materials and environmental contexts, and they offer useful direction for further study of clays and their intricate interactions.

Acknowledgements CM acknowledges WO for the original idea for the study, the fruitful discussions about the XRD modeling approach, and the montmorillonite hydration behavior.

Authors' Contributions PhD student Chadha Mejri (CM) realized the experimental part, the XRD profile modeling approach and drafting of the manuscript. Dr. Walid Oueslati (WO) supervised the study, contributed to the drafting of the manuscript, and to proof reading/revision. A. Ben Haj Amara conceived and designed the experiments, and played a key role in planning and conceptualizing the research.

Funding This research received no specific grant from any funding agency in the public, commercial, or not-for-profit sectors.

Data Availability The generated and analyzed data during the current study are included within the article and can be obtained from the corresponding authors upon reasonable request.

Declarations

Disclosure The results presented are a part of the PhD thesis of Chadha Mejri carried out at the Faculty of Sciences of Bizerte, University of Carthage, 7021 Zarzouna, Tunisia and supervised by Dr Walid Oueslati.

Consent for Publication The authors agree to publication in *Clays and Clay Minerals*.

Conflicts of Interest The authors declare no conflict of interest.

References

Abadie, P.M. (2020). La gestion des déchets radioactifs en France et dans le monde. In *Annales des Mines-Responsabilite et environnement*,https://doi.org/10.3917/re1.097.0048

Ahmed, H. A., Soliman, M. S., & Othman, S. A. (2021). Synthesis and characterization of magnetic nickel ferrite-modified montmorillonite nanocomposite for Cu (II) and Zn (II) ions removal from wastewater. *Egyptian Journal of Chemistry, 64*, 5627–5645. https://doi.org/10.21608/ejchem.2021.69597.3527

Alshabanat, M., Al-Arrash, A., & Mekhamer, W. (2013). Polystyrene/montmorillonite nanocomposites: Study of the morphology and effects of sonication time on thermal stability. *Journal of Nanomaterials, 2013*, 650725. https://doi.org/10.1155/2013/650725

Altin, O., Ozbelge, O. H., & Dogu, T. (1999). Effect of pH, flow rate and concentration on the sorption of Pb and Cd on montmorillonite: I. Experimental. *Journal of Chemical Technology & Biotechnology, 74*(12), 1131–1138. https://doi.org/10.1002/(SICI)1097-4660(199912)74:12%3c1131::AID-JCTB158%3e3.0.CO;2-0

Altin, O., Ozbelge, O. H., & Dogu, T. (1999). Effect of pH, flow rate and concentration on the sorption of Pb and Cd on montmorillonite: II. Modelling. *Journal of Chemical Technology & Biotechnology, 74*(12), 1139–1144. https://doi.org/10.1002/(SICI)1097-4660(199912)74:12%3c1139::AID-JCTB159%3e3.0.CO;2-Q

Amara, A. B. H. (1997). X-ray diffraction, infrared and TGA/DTG analysis of hydrated nacrite. *Clay Minerals, 32*(3), 463–470. https://doi.org/10.1180/claymin.1997.032.3.08

Ammar, M., Oueslati, W., & Ben Haj Amara, A. (2018). Mg-Exchanged Montmorillonite Undergoing External Environmental Solicitation: Crystalline Swelling Process Investigation. In *Conference of the Arabian Journal of Geosciences*,https://doi.org/10.1007/978-3-030-01575-6_44

Ammar, M., Oueslati, W., Ben Rhaiem, H., & Ben Haj Amara, A. (2014c). Quantitative XRD analysis of the dehydration–hydration performance of (Na^+, Cs^+) exchanged smectite. *Desalination and Water Treatment, 52*(22–24), 4314–33. https://doi.org/10.1080/19443994.2013.803324

Ammar, M., Oueslati, W., Chorfi, N., & Rhaiem, H. B. (2014a). Interlamellar space configuration under variable environmental conditions in the case of Ni-exchanged montmorillonite: Quantitative XRD analysis. *Journal of Nanomaterials, 2014*, 284612. https://doi.org/10.1155/2014/284612

Ammar, M., Oueslati, W., Rhaiem, H. B., & Amara, A. B. H. (2014b). Effect of the hydration sequence orientation on the structural properties of Hg exchanged montmorillonite: Quantitative XRD analysis. *Journal of Environmental Chemical Engineering, 2*(3), 1604–1611. https://doi.org/10.1016/j.jece.2014.05.022

Anastácio, A. S., Aouad, A., Sellin, P., Fabris, J. D., Bergaya, F., & Stucki, J. W. (2008). Characterization of a redox-modified clay mineral with respect to its suitability as a barrier in radioactive waste confinement. *Applied Clay Science, 39*(3–4), 172–179. https://doi.org/10.1016/j.clay.2007.05.007

Antoine, P., Marchiol, A., Brocandel, M., & Gros, Y. (2005). Découverte de structures périglaciaires (sand-wedges et composite-wedges) sur le site de stockage de déchets radioactifs de l'Aube (France). *Comptes Rendus Geoscience, 337*(16), 1462–1473. https://doi.org/10.1016/j.crte.2005.08.008

Babel, S., & Kurniawan, T. A. (2003). Low-cost adsorbents for heavy metals uptake from contaminated water: A review. *Journal of Hazardous Materials, 97*(1–3), 219–243. https://doi.org/10.1016/S0304-3894(02)00263-7

Bailey, S.W. (1980). Structures of layer silicates. In: *Crystal Structures of Clay Minerals and their X-Ray Identification* (Ed.), Mineralogical Society of Great Britain and Ireland.

Bataillon, C., Musy, C., & Roy, M. (2001). Corrosion des surconteneurs de déchets, cas d'un surconteneur en acier faiblement allié. *Le Journal De Physique IV, 11*,. https://doi.org/10.1051/jp4:2001127

Ben Brahim, J., Besson, G., & Tchoubar, C. (1984). Etude des profils des bandes de diffraction X d'une beidellite-Na

hydratée à deux couches d'eau. Détermination du mode d'empilement des feuillets et des sites occupés par l'eau. *Journal of Applied Crystallography, 17*(9), 179–188. https://doi.org/10.1107/S0021889884011262

Berend, I. (1991). *Les mécanismes d'hydratation de montmorillonites homoioniques pour des pressions relatives inferieures à 0.95* (Doctoral dissertation, Institut National Polytechnique de Lorraine).

Bérend, I., Cases, J. M., François, M., Uriot, J. P., Michot, L., Masion, A., & Thomas, F. (1995). Mechanism of adsorption and desorption of water vapor by homoionic montmorillonites: 2. The Li+ Na+, K+, Rb+ and Cs+-exchanged forms. *Clays and Clay Minerals, 43*(3), 324–336. https://doi.org/10.1346/CCMN.1995.0430307

Bergaya, F.B.K.G., & Lagaly, G. (2013). General introduction: clays, clay minerals, and clay science. In Developments in clay science (Ed.), *Handbook of Clay Science* (pp. 1–19). Elsevier.

Bobin, J.L., Huffer, E., & Nifenecker, H. (2021). 20-LE STOCKAGE DES DÉCHETS NUCLÉAIRES EN SITE PROFOND. In *L'énergie de demain (Ed.)*, (pp. 429–448). EDP Sciences.

Brown, G. (1982). *Crystal Structures of Clay Minerals and their X-ray identification.* The Mineralogical Society of Great Britain and Ireland.

Carretero, M. I., & Pozo, M. (2009). Clay and non-clay minerals in the pharmaceutical industry: Part I. Excipients and medical applications. *Applied Clay Science, 46*(1), 73–80. https://doi.org/10.1016/j.clay.2009.07.017

Carretero, M. I., & Pozo, M. (2010). Clay and non-clay minerals in the pharmaceutical and cosmetic industries Part II Active ingredients. *Applied Clay Science, 47*(3–4), 171–181. https://doi.org/10.1016/j.clay.2009.10.016

Cases, J. M., Bérend, I., François, M., Uriot, L. P., Michot, L. J., & Thomas, F. (1997). Mechanism of adsorption and desorption of water vapor by homoionic montmorillonite: 3. The Mg^{2+}, Ca^{2+}, Sr^{2+} and Ba^{2+} exchanged forms. *Clays and Clay Minerals, 45*, 8–22. https://doi.org/10.1346/CCMN.1997.0450102

Chaari, I., Medhioub, M., & Jamoussi, F. (2011). Use of clay to remove heavy metals from Jebel Chakir landfill leachate. *Journal of Applied Sciences in Environmental Sanitation, 6*(2), 143–148.

Chalghaf, R., Oueslati, W., Ammar, M., Rhaiem, H. B., & Amara, A. B. H. (2012). Effect of an "in situ" hydrous strain on the ionic exchange process of dioctahedral smectite: Case of solution containing (Cu^{2+}, Co^{2+}) cations. *Applied Surface Science, 258*(22), 9032–9040. https://doi.org/10.1016/j.apsusc.2012.05.144

Chalghaf, R., Oueslati, W., Ammar, M., Rhaiem, H. B., & Amara, A. B. H. (2013). Effect of temperature and pH value on cation exchange performance of a natural clay for selective (Cu^{2+}, Co^{2+}) removal: Equilibrium, sorption and kinetics. *Progress in Natural Science: Materials International, 23*(1), 23–35. https://doi.org/10.1016/j.pnsc.2013.01.004

Coles, C. A., & Yong, R. N. (2002). Aspects of kaolinite characterization and retention of Pb and Cd. *Applied Clay Science, 22*(1–2), 39–45. https://doi.org/10.1016/S0169-1317(02)00110-2

Cui, J., Zhang, Z., & Han, F. (2020). Effects of pH on the gel properties of montmorillonite, palygorskite and montmorillonite-palygorskite composite clay. *Applied Clay Science, 190*, 105543. https://doi.org/10.1016/j.clay.2020.105543

Dazas, B., Ferrage, E., Delville, A., & Lanson, B. (2014). Interlayer structure model of tri-hydrated low-charge smectite by X-ray diffraction and Monte Carlo modeling in the Grand Canonical ensemble. *American Mineralogist, 99*, 1724–1735. https://doi.org/10.2138/am.2014.4846

Dazas, B., Lanson, B., Delville, A., Robert, J. L., Komarneni, S., Michot, L. J., & Ferrage, E. (2015). Influence of tetrahedral layer charge on the organization of interlayer water and ions in synthetic Na-saturated smectites. *The Journal of Physical Chemistry C, 119*(8), 4158–4172. https://doi.org/10.1021/jp5123322

De Queiroga, L. N. F., Franca, D. B., Rodrigues, F., Santos, I. M., Fonseca, M. G., & Jaber, M. (2019). Functionalized bentonites for dye adsorption: Depollution and production of new pigments. *Journal of Environmental Chemical Engineering, 7*(5), 103333. https://doi.org/10.1016/j.jece.2019.103333

Dizier, A. (2011). Caractérisation des effets de température dans la zone endommagée autour de tunnels de stockage de déchets nucléaires dans des roches argileuses.

Drits, V.A., & Tchoubar, C. (1990). The modelization method in the determination of the structural characteristics of some layer silicates: Internal structure of the layers, nature and distribution of the stacking faults. In *X-ray Diffraction by Disordered Lamellar Structures* (pp. 233–303). Springer, Berlin, Heidelberg.

Es-Sahbany, H., Berradi, M., Nkhili, S., Hsissou, R., Allaoui, M., Loutfi, M., & El Youbi, M. S. (2019). Removal of heavy metals (nickel) contained in wastewater-models by the adsorption technique on natural clay. *Materials Today: Proceedings, 13*, 866–875. https://doi.org/10.1016/j.matpr.2019.04.050

Ferrage, E. (2016). Investigation of the interlayer organization of water and ions in smectite from the combined use of diffraction experiments and molecular simulations. A review of methodology, applications, and perspectives. *Clays and Clay Minerals, 64*(4), 348–373. https://doi.org/10.1346/CCMN.2016.0640401

Ferrage, E., Kirk, C. A., Cressey, G., & Cuadros, J. (2007). Dehydration of Ca-montmorillonite at the crystal scale Part I: Structure evolution. *American Mineralogist, 92*(7), 994–1006. https://doi.org/10.2138/am.2007.2396

Ferrage, E., Kirk, C. A., Cressey, G., & Cuadros, J. (2007). Dehydration of Ca-montmorillonite at the crystal scale. Part 2. Mechanisms and kinetics. *American Mineralogist, 92*(7), 1007–1017. https://doi.org/10.2138/am.2007.2397

Ferrage, E., Lanson, B., Malikova, N., Plançon, A., Sakharov, B. A., & Drits, V. A. (2005b). New insights on the distribution of interlayer water in bi-hydrated smectite from X-ray diffraction profile modeling of 00l reflections. *Chemistry of Materials, 17*(13), 3499–3512. https://doi.org/10.1021/cm047995v

Ferrage, E., Lanson, B., Michot, L. J., & Robert, J. L. (2010). Hydration properties and interlayer organization of water and ions in synthetic Na-smectite with tetrahedral layer charge. Part 1. Results from X-ray diffraction

profile modeling. *The Journal of Physical Chemistry C, 114*(10), 4515–4526. https://doi.org/10.1021/jp909860p

Ferrage, E., Lanson, B., Sakharov, B. A., & Drits, V. A. (2005). Investigation of smectite hydration properties by modeling experimental X-ray diffraction patterns: Part I. *Montmorillonite hydration properties. American Mineralogist, 90*(8–9), 1358–1374. https://doi.org/10.2138/am.2005.1776

Gomes, C. D. S. F., & Silva, J. B. P. (2007). Minerals and clay minerals in medical geology. *Applied Clay Science, 36*(1–3), 4–21. https://doi.org/10.1016/j.clay.2006.08.006

Gregoire, B., Dazas, B., Leloup, M., Hubert, F., Tertre, E., Ferrage, E., & Petit, S. (2020). Optical theory-based simulation of attenuated total reflection infrared spectra of montmorillonite films. *Clays and Clay Minerals, 68*, 175–187. https://doi.org/10.1007/s42860-020-00073-x

Gubitosa, J., Rizzi, V., Fini, P., & Cosma, P. (2019). Hair care cosmetics: From traditional shampoo to solid clay and herbal shampoo, a review. *Cosmetics, 6*, 1–13. https://doi.org/10.3390/cosmetics6010013

Güven, N., & Bailey, S. W. (1988). Hydrous Phyllosilicates. *Reviews in Mineralogy, 19*, 497–559.

Hu, C., Zhu, P., Cai, M., Hu, H., & Fu, Q. (2017). Comparative adsorption of Pb (II), Cu (II) and Cd (II) on chitosan saturated montmorillonite: Kinetic, thermodynamic and equilibrium studies. *Applied Clay Science, 143*, 320–326. https://doi.org/10.1016/j.clay.2017.04.005

Huber, F. M., Heck, S., Truche, L., Bouby, M., Brendlé, J., Hoess, P., & Schäfer, T. (2015). Radionuclide desorption kinetics on synthetic Zn/Ni-labeled montmorillonite nanoparticles. *Geochimica et Cosmochimica Acta, 148*, 426–441. https://doi.org/10.1016/j.gca.2014.10.010

Hussain, S. T., & Ali, S. A. K. (2021). Removal of heavy metal by ion exchange using bentonite clay. *Journal of Ecological Engineering, 22*(1), 104–111. https://doi.org/10.12911/22998993/128865

Ishidera, T., Okazaki, M., Yamada, Y., Tomura, T., & Shibutani, S. (2022). Sorption of Sn and Nb on montmorillonite at neutral to alkaline pH. *Journal of Nuclear Science and Technology, 60*(5), 536–546. https://doi.org/10.1080/00223131.2022.2125453

Jiang, K., Liu, K., Peng, Q., & Zhou, M. (2021). Adsorption of Pb (II) and Zn (II) ions on humus-like substances modified montmorillonite. *Colloids and Surfaces A: Physicochemical and Engineering Aspects, 631*, 127706. https://doi.org/10.1016/j.colsurfa.2021.127706

Karmous, M. S., Ben Rhaiem, H., Naamen, S., Oueslati, W., & Ben Haj Amara, A. (2006). The interlayer structure and thermal behavior of Cu and Ni montmorillonites. *Zeitschrift Für Kristallographie Supplement, 23*(2006), 431–436.

Karmous, M. S., Rhaiem, H. B., Robert, J. L., Lanson, B., & Amara, A. B. H. (2009). Charge location effect on the hydration properties of synthetic saponite and hectorite saturated by Na^{+}, Ca^{2+} cations: XRD investigation. *Applied Clay Science, 46*(1), 43–50. https://doi.org/10.1016/j.clay.2009.07.007

Komadel, P., Bujdák, J., Madejová, J., Šucha, V., & Elsass, F. (1996). Effect of non-swelling layers on the dissolution of reduced-charge montmorillonite in hydrochloric acid. *Clay Minerals, 31*(3), 333–345. https://doi.org/10.1180/claymin.1996.031.3.04

Kozaki, T., Sawaguchi, T., Fujishima, A., & Sato, S. (2010). Effect of exchangeable cations on apparent diffusion of Ca^{2+} ions in Na-and Ca-montmorillonite mixtures. *Physics and Chemistry of the Earth, Parts A/B/C, 35*(6–8), 254–258. https://doi.org/10.1016/j.pce.2010.04.006

Kraevsky, S. V., Tournassat, C., Vayer, M., Warmont, F., Grangeon, S., Wakou, B. F. N., & Kalinichev, A. G. (2020). Identification of montmorillonite particle edge orientations by atomic-force microscopy. *Applied Clay Science, 186*, 105442. https://doi.org/10.1016/j.clay.2020.105442

Kretz, R. (1983). Symbols for rock-forming minerals. *American Mineralogist*.

Lahbib, M., Meftah, M., Mejri, C., Oueslati, W., & Amara, A. B. H. (2023). The starting stoichiometry, keys parameter to enhance the intrinsic microstructural and functional properties of synthesized hybrid nanocomposites chitosan/Na-montmorillonite/ZnO nanoparticlest type. *Applied Surface Science Advances, 13*, 100369. https://doi.org/10.1016/j.apsadv.2023.100369

Landrein, P., Vigneron, G., Delay, J., Lebon, P., & Pagel, M. (2013). Lithologie, hydrodynamisme et thermicité dans le système sédimentaire multicouche recoupé par les forages Andra de Montiers-sur-Saulx (Meuse). *Bulletin De La Société Géologique De France, 184*(6), 519–543. https://doi.org/10.2113/gssgfbull.184.6.519

Lanson, B. (2011). Modelling of X-ray diffraction profiles: Investigation of defective lamellar structure crystal chemistry. In *Layered Mineral Structures and their Application in Advanced Technologies* (Ed.), European Mineralogical Union and the Mineralogical Society of Great Britain and Ireland.

Lanson, B. (2005). Crystal structure of mixed-layer minerals and their X-ray identification: New insights from X-ray diffraction profile modeling. *Clay Science, 12*(Supplement1), 1–5. https://doi.org/10.11362/jcssjclayscience1960.12.Supplement1_1

Laverov, N. P., Yudintsev, S. V., Kochkin, B. T., & Malkovsky, V. I. (2016). The Russian strategy of using crystalline rock as a repository for nuclear waste. *Elements*. https://doi.org/10.2113/gselements.12.4.253

Leong, Y. K., Du, M., Au, P. I., Clode, P., & Liu, J. (2018). Microstructure of sodium montmorillonite gels with long aging time scale. *Langmuir, 34*(33), 9673–9682. https://doi.org/10.1021/acs.langmuir.8b00213

Leoni, M. (2008). Diffraction analysis of layer disorder. *Zeitschrift Für Kristallographie, 223*(9), 561–568. https://doi.org/10.1524/zkri.2008.1214

Liu, L., Zhang, C., Jiang, W., Li, X., Dai, Y., & Jia, H. (2021). Understanding the sorption behaviors of heavy metal ions in the interlayer and nanopore of montmorillonite: A molecular dynamics study. *Journal of Hazardous Materials, 416*, 125976. https://doi.org/10.1016/j.jhazmat.2021.125976

Liu, X., & Yang, G. (2022). Mechanisms for cation exchange at the interfaces of montmorillonite nanoparticles: Insights for Pb^{2+} control. *Colloids and Surfaces A: Physicochemical and Engineering Aspects, 641*, 128556. https://doi.org/10.1016/j.colsurfa.2022.128556

Mahy, J. G., Tsaffo Mbognou, M. H., Léonard, C., Fagel, N., Woumfo, E. D., & Lambert, S. D. (2022). Natural Clay Modified with ZnO/TiO_2 to Enhance Pollutant Removal from Water. *Catalysts, 12*(2), 148. https://doi.org/10.3390/catal12020148

Manohar, D. M., Krishnan, K. A., & Anirudhan, T. S. (2002). Removal of mercury (II) from aqueous solutions and chlor-alkali industry wastewater using 2-mercaptobenzimidazole-clay. *Water Research, 36*(6), 1609–1619. https://doi.org/10.1016/S0043-1354(01)00362-1

Marty, N. C., Grangeon, S., Lassin, A., Madé, B., Blanc, P., & Lanson, B. (2020). A quantitative and mechanistic model for the coupling between chemistry and clay hydration. *Geochimica et Cosmochimica Acta, 283*, 124–135. https://doi.org/10.1016/j.gca.2020.05.029

Massaro, M., Lazzara, G., Milioto, S., Noto, R., & Riela, S. (2017). Covalently modified halloysite clay nanotubes: Synthesis, properties, biological and medical applications. *Journal of Materials Chemistry B, 5*(16), 2867–2882. https://doi.org/10.1039/C7TB00316A

Meftah, M., Oueslati, W., & Amara, A.B.H. (2010). Synthesis of zeolites A and P from 1: 1 and HS from 2: 1 clays. In *IOP Conference Series: Materials Science and Engineering*, *13(1)*, (p. 1–8). IOP Publishing.

Meftah, M., Oueslati, W., & Amara, A. B. H. (2011). XRD and MAS NMR investigation of synthesized zeolite from 2: 1 Tunisian clays: Effect of concentration of NaOH solution on the final product nature. *Zeithshrift für Kristallographie, Proceedings, 1*, 467–472. https://doi.org/10.1524/zkpr.2011.0071

Mejri, C., Oueslati, W., Ben Haj & Amara, A. (2022a). Effect of layer type distribution within the crystallite on the diffracted (00ℓ) theoretical intensities. *In E3S Web of Conferences, EDP* Sciences, https://doi.org/10.1051/e3sconf/202235403009

Mejri, C., Oueslati, W., & Amara, A. B. H. (2021). How the Solid/Liquid Ratio Affects the Cation Exchange Process and Porosity in the Case of Dioctahedral Smectite: Structural Analysis? *Adsorption Science & Technology, 2021*, 9732092. https://doi.org/10.1155/2021/9732092

Mejri, C., Oueslati, W., & Amara, A. B. H. (2022b). Structural Alteration, Hydration Stability, Heavy Metal Removal Efficiency, and Montmorillonite Porosity Fate by Coupling the Soil Solution pH and a Thermal Gradient. *Adsorption Science & Technology, 2022*, 4421932. https://doi.org/10.1155/2022/4421932

Mejri, C., Oueslati, W., & Amara, A. B. H. (2023). Structure and reactivity assessment of dioctahedral montmorillonite during provoked variable sequential cation exchange process via XRD modelling approach. *Applied Surface Science Advances, 15*, 100403. https://doi.org/10.1016/j.apsadv.2023.100403

Mermut, A. R., & Cano, A. F. (2001). Baseline studies of the clay minerals society source clays: Chemical analyses of major elements. *Clays and Clay Minerals, 49*(5), 381–386.

Moldoveanu, G., & Papangelakis, V. (2021). Chelation-assisted ion-exchange leaching of rare earths from clay minerals. *Metals, 11*(8), 1265. https://doi.org/10.3390/met11081265

Moll, W. F., Jr. (2001). Baseline studies of the clay minerals society source clays: Geological origin. *Clays and Clay Minerals, 49*(5), 374–380.

Momeni, M., Bayat, M., & Ajalloeian, R. (2022). Laboratory investigation on the effects of pH-induced changes on geotechnical characteristics of clay soil. *Geomechanics and Geoengineering, 17*(1), 188–196. https://doi.org/10.1080/17486025.2020.1716084

Mousavi, S.M., Hashemi, S.A., Salahi, S., Hosseini, M., Amani, A.M., & Babapoor, A. (2018). *Development of clay nanoparticles toward bio and medical applications* (pp. 167–191). London, UK: IntechOpen.

Neves, H. S. D. C., da Silva, T. L., da Silva, M. G. C., Guirardello, R., & Vieira, M. G. A. (2022). Ion exchange and adsorption of cadmium from aqueous media in sodium-modified expanded vermiculite. *Environmental Science and Pollution Research, 29*(53), 79903–79919. https://doi.org/10.1007/s11356-021-16841-8

Newman, A. C. (Ed.). (1987). *Chemistry of Clays and Clay Minerals*. Mineralogical Society of Great Britain & Ireland.

Nistor, I., & Miron, N. (2007). Depollution of uranyl polluted waters using pillared clays. *Journal of Thermal Analysis and Calorimetry, 89*, 977–981. https://doi.org/10.1007/s10973-006-7701-4

Ohkubo, T., Okamoto, T., Kawamura, K., Guégan, R., Deguchi, K., Ohki, S., Shimizu, T., Tachi, Y., & Iwadate, Y. (2018). New insights into the Cs adsorption on montmorillonite clay from ^{133}Cs solid-state NMR and density functional theory calculations. *The Journal of Physical Chemistry A, 122*(48), 9326–9337. https://doi.org/10.1021/acs.jpca.8b07276

Otunola, B. O., & Ololade, O. O. (2020). A review on the application of clay minerals as heavy metal adsorbents for remediation purposes. *Environmental Technology & Innovation, 18*, 100692. https://doi.org/10.1016/j.eti.2020.100692

Oueslati, W. (2019). Effect of soil solution pH during the tetracycline intercalation on the structural properties of a dioctahedral smectite: Microstructural analysis. *Journal of Nanomaterials, 2019*, 7414039. https://doi.org/10.1155/2019/7414039

Oueslati, W., Ammar, M., & Chorfi, N. (2015). Quantitative XRD analysis of the structural changes of Ba-exchanged montmorillonite: Effect of an in situ hydrous perturbation. *Minerals, 5*(3), 507–526. https://doi.org/10.3390/min5030507

Oueslati, W., Ben Rhaiem, H., Karmous, M. S., Naaman, S., & Ben Haj Amara, A. (2006). Study of the structural evolution and selectivity of Wyoming montmorillonite in relation with the concentration of Cu^{2+} and Ni^{2+}. *Zeitschrift Für Kristallographie, Supplement, 23*, 425–429. https://doi.org/10.1524/zksu.2006.suppl_23.425

Oueslati, W., Chorfi, N., & Abdelwahed, M. (2017). Effect of mechanical constraint on the hydration properties of Na-montmorillonite: Study under extreme relative humidity conditions. *Powder Diffraction, 32*(S1), S160–S167.

Oueslati, W., Karmous, M. S., Rhaiem, H. B., Lanson, B., & Amara, A. B. H. (2007). Effect of interlayer cation and relative humidity on the hydration properties of a

dioctahedral smectite. *Zeitschrift Für Kristallographie, Supplement, 26*, 417–422.

Oueslati, W., & Meftah, M. (2018). Discretization of the water uptake process of Na-montmorillonite undergoing atmospheric stress: XRD modeling approach. *Advances in Materials Science and Engineering, 2018*, 5219624. https://doi.org/10.1155/2018/5219624

Oueslati, W., Mefath, M., Rhaiem, H. B., & Amara, A. B. H. (2009). Cation exchange selectivity versus concentration of competing heavy metal cations (Pb^{2+}, Zn^{2+}): Case of Na-montmorillonite. *Physics Procedia, 2*(3), 1059–1063. https://doi.org/10.1016/j.phpro.2009.11.063

Oueslati, W., Mejri, C., & Amara, A.B.H. (2022a). X-ray Diffraction Profiles Modeling Method for Layered Structures Reconstruction: Nanoclay Structural Verification. In Nanoclay - Recent Advances, New Perspectives and Applications (Ed.), *Intechopen* (pp. 2–23). https://www.intechopen.com/chapters/83630

Oueslati, W., Mejri, C., & Ben Haj Amara, A. (2022b). Impact of Uniaxial Mechanical Perturbation on Structural Properties and Smectite Porosity Features: Ion Exchanger Efficiency and Adsorption Performance Fate. *Advances in Civil Engineering, 2022*, 4441705. https://doi.org/10.1155/2022/4441705

Oueslati, W., Rhaiem, H. B., & Amara, A. B. H. (2011). XRD investigations of hydrated homoionic montmorillonite saturated by several heavy metal cations. *Desalination, 271*(1–3), 139–149. https://doi.org/10.1016/j.desal.2010.12.018

Oueslati, W., Rhaiem, H. B., & Amara, A. B. H. (2012). Effect of relative humidity constraint on the metal exchanged montmorillonite performance: An XRD profile modeling approach. *Applied Surface Science, 261*, 396–404. https://doi.org/10.1016/j.apsusc.2012.08.022

Panchal, A., Fakhrullina, G., Fakhrullin, R., & Lvov, Y. (2018). Self-assembly of clay nanotubes on hair surface for medical and cosmetic formulations. *Nanoscale, 10*, 18205. https://doi.org/10.1039/C8NR05949G

Papadopoulos, A., Giouri, K., Tzamos, E., Filippidis, A., & Stoulos, S. (2014). Natural radioactivity and trace element composition of natural clays used as cosmetic products in the Greek market. *Clay Minerals, 49*(1), 53–62. https://doi.org/10.1180/claymin.2014.049.1.05

Potgieter, J. H., Potgieter-Vermaak, S. S., & Kalibantonga, P. D. (2006). Heavy metals removal from solution by palygorskite clay. *Minerals Engineering, 19*(5), 463–470. https://doi.org/10.1016/j.mineng.2005.07.004

Pufahl, D. E., Fredlund, D. G., & Rahardjo, H. (1983). Lateral earth pressures in expansive clay soils. *Canadian Geotechnical Journal, 20*(2), 228–241. https://doi.org/10.1139/t83-027

Pusch, R., Knutsson, S., Al-Taie, L., & Hatem, M. (2012). Optimal ways of disposal of highly radioactive waste. *Natural Science, 4*(11A), 906–918. https://doi.org/10.4236/ns.2012.431118

Sakharov, B.A., & Lanson, B. (2013). X-ray identification of mixed-layer structures: modelling of diffraction effects. In Developments in Clay Science (Ed.), *Handbook of Clay Science* (pp. 51–135). Elsevier.

Sakharov, B. A., & Drits, V. A. (1973). Mixed-layer kaolinite-montmorillonite: A comparison of observed and calculated diffraction patterns. *Clays and Clay Minerals, 21*, 15–17. https://doi.org/10.1346/CCMN.1973.0210104

Saravanan, S., Ramamurthy, P. C., & Madras, G. (2015). Effects of temperature and clay content on water absorption characteristics of modified MMT clay/cyclic olefin copolymer nanocomposite films: Permeability, dynamic mechanical properties and the encapsulated organic device performance. *Composites Part B: Engineering, 73*, 1–9. https://doi.org/10.1016/j.compositesb.2014.12.030

Sato, T., Watanabe, T., & Otsuka, R. (1992). Effects of layer charge, charge location, and energy change on expansion properties of dioctahedral smectites. *Clays and Clay Minerals, 40*, 103–113. https://doi.org/10.1346/CCMN.1992.0400111

Scardi, P., & Leoni, M. (2002). Whole powder pattern modelling. *Acta Crystallographica Section A: Foundations of Crystallography, 58*(2), 190–200. https://doi.org/10.1107/S0108767301021298

Scardi, P., Leoni, M., & Beyerlein, K. R. (2011). On the modelling of the powder pattern from a nanocrystalline material. *Zeitschrift Für Kristallographie, 226*(12), 924–933. https://doi.org/10.1524/zkri.2011.1448

Scholtzová, E., & Tunega, D. (2019). Density functional theory study of the stability of the tetrabutylphosphonium and tetrabutylammonium montmorillonites. *Clay Minerals, 54*(1), 41–48. https://doi.org/10.1180/clm.2019.5

Schroeder, P. A., Pruett, R. J., & Melear, N. D. (2004). Crystal-chemical changes in an oxidative weathering front in a Georgia kaolin deposit. *Clays and Clay Minerals, 52*, 211–220. https://doi.org/10.1346/CCMN.2004.0520207

Segad, M., Jonsson, B., Åkesson, T., & Cabane, B. (2010). Ca/Na montmorillonite: Structure, forces and swelling properties. *Langmuir, 26*(8), 5782–5790. https://doi.org/10.1021/la9036293

Sellin, P., & Leupin, O. X. (2013). The use of clay as an engineered barrier in radioactive-waste management–a review. *Clays and Clay Minerals, 61*(6), 477–498. https://doi.org/10.1346/CCMN.2013.0610601

Shannon, R. D. (1976). Revised effective ionic radii and systematic studies of interatomic distances in halides and chalcogenides. *Acta Crystallographica Section A: Crystal Physics, Diffraction, Theoretical and General Crystallography, 32*(5), 751–767. https://doi.org/10.1107/S0567739476001551

Shi, Y., Zhong, S., Wang, X., & Feng, C. (2022). A review of the removal of heavy metal ions in wastewater by modified montmorillonite. *Water Policy, 24*(10), 1590–1609. https://doi.org/10.2166/wp.2022.033

Sun, L., Hirvi, J. T., Schatz, T., Kasa, S., & Pakkanen, T. A. (2015). Estimation of montmorillonite swelling pressure: A molecular dynamics approach. *The Journal of Physical Chemistry C, 119*(34), 19863–19868. https://doi.org/10.1021/acs.jpcc.5b04972

Tan, J., Li, Y., Xia, L., Li, H., Song, S., Wu, L., & Farías, M. E. (2022). Enhancement of Cd (II) Adsorption on Microalgae-Montmorillonite Composite. *Arabian Journal for Science and Engineering, 47*(6), 6715–6727. https://doi.org/10.1007/s13369-021-063-y

Tan, S. Z., Zhang, K. H., Zhang, L. L., Xie, Y. S., & Liu, Y. L. (2008). Preparation and characterization of the

antibacterial Zn^{2+} or/and Ce^{3+} loaded montmorillonites. *Chinese Journal of Chemistry, 26*(5), 865–869. https://doi.org/10.1002/cjoc.200890160

Tlemsani, S., Taleb, Z., Piraúlt-Roy, L., & Taleb, S. (2022). Temperature and pH influence on Diuron adsorption by Algerian Mont-Na Clay. International Journal of Environmental Analytical Chemistryhttps://doi.org/10.1080/03067319.2022.2060093

Tournassat, C., Grangeon, S., Leroy, P., & Giffaut, E. (2013). Modeling specific pH dependent sorption of divalent metals on montmorillonite surfaces. A review of pitfalls, recent achievements and current challenges. *American Journal of Science*, https://www.ajsonline.org/content/313/5/395.short

Tournassat, C., Davis, J. A., Chiaberge, C., Grangeon, S., & Bourg, I. C. (2016). Modeling the acid–base properties of montmorillonite edge surfaces. *Environmental Science & Technology, 50*(24), 13436–13445. https://doi.org/10.1021/acs.est.6b04677

Usman, A. R. A., Kuzyakov, Y., & Stahr, K. (2004). Effect of clay minerals on extractability of heavy metals and sewage sludge mineralization in soil. *Chemistry and Ecology, 20*(2), 123–135. https://doi.org/10.1080/02757540410001665971

Vidal, O., Baldeyrou, A., Beaufort, D., Fritz, B., Geoffroy, N., & Lanson, B. (2012). Experimental study of the stability and phase relations of clays at high temperature in a thermal gradient. *Clays and Clay Minerals, 60*, 200–225. https://doi.org/10.1346/CCMN.2012.0600209

Wahba, M.M., Labib, B.F., Darwish, K.H.M., & Zaghloul, M.A. (2017). Application of some clay minerals to eliminate the hazards of heavy metals in contaminated soils. In *15th International conference on environmental science and technology, CEST*.

Wakou, B.N., & Kalinichev, A.G. (2012). Molecular modeling of the swelling properties and interlayer structure of Cs, Na, K-Montmorillonite: Effects of charge distribution in the clay layers. *In 5th International meeting Clays in Natural and Engineered Barriers for Radioactive Waste Confinement*.

Warr, L. N. (2020). Recommended abbreviations for the names of clay minerals and associated phases. *Clay Minerals, 55*(3), 261–264. https://doi.org/10.1180/clm.2020.30

Whitney, D. L., & Evans, B. W. (2010). Abbreviations for names of rock-forming minerals. *American Mineralogist, 95*(1), 185–187. https://doi.org/10.2138/am.2010.3371

Whittaker, M. L., Lammers, L. N., Carrero, S., Gilbert, B., & Banfield, J. F. (2019). Ion exchange selectivity in clay is controlled by nanoscale chemical–mechanical coupling. *Proceedings of the National Academy of Sciences, 116*(44), 22052–22057. https://doi.org/10.1073/pnas.1908086116

Wu, M., Bi, E., & Li, B. (2022). Cotransport of nano-hydroxyapatite and different Cd (II) forms influenced by fulvic acid and montmorillonite colloids. *Water Research, 218*, 118511. https://doi.org/10.1016/j.watres.2022.118511

Yan, H., & Zhang, Z. (2021). Effect and mechanism of cation species on the gel properties of montmorillonite. *Colloids and Surfaces A: Physicochemical and Engineering Aspects, 611*, 125824. https://doi.org/10.1016/j.colsurfa.2020.125824

Yin, H., & Zhu, J. (2016). In situ remediation of metal contaminated lake sediment using naturally occurring, calcium-rich clay mineral-based low-cost amendment. *Chemical Engineering Journal, 285*, 112–120. https://doi.org/10.1016/j.cej.2015.09.108

Yingying, S., Baoqiang, Z., & Yang, W.(2020). Application of clay minerals in remediation of heavy metal pollution in soil. In *E3S Web of Conferences* . EDP Sciences, https://doi.org/10.1051/e3sconf/202020401011

Yotsuji, K., Tachi, Y., Sakuma, H., & Kawamura, K. (2021). Effect of interlayer cations on montmorillonite swelling: Comparison between molecular dynamic simulations and experiments. *Applied Clay Science, 204*, 106034. https://doi.org/10.1016/j.clay.2021.106034

Yuan, G.D., Theng, B.K.G., Churchman, G.J., & Gates, W.P. (2013). Clays and clay minerals for pollution control. In *Developments in Clay Science* (pp. 587–644). Elsevier.

Zhang, C., Liu, L., Dai, Y., Zhu, K., Liu, Z., & Jia, H. (2022). Molecular dynamics simulations of exchange behavior of radionuclides into montmorillonite: Unraveling the dynamic processes and microscopic structures. *Applied Clay Science, 226*, 106579. https://doi.org/10.1016/j.clay.2022.106579

Zhang, C., Liu, X., Tinnacher, R. M., & Tournassat, C. (2018). Mechanistic understanding of uranyl ion complexation on montmorillonite edges: A combined first-principles molecular dynamics–surface complexation modeling approach. *Environmental Science & Technology, 52*(15), 8501–8509. https://doi.org/10.1021/acs.est.8b02504

Zhang, W., An, Y., Li, S., Liu, Z., Chen, Z., Ren, Y., Wang, S., Zhang, X., & Wang, X. (2020). Enhanced heavy metal removal from an aqueous environment using an eco-friendly and sustainable adsorbent. *Scientific Reports, 10*(1), 16453. https://doi.org/10.1038/s41598-020-73570-7

Zhang, Y., Li, Y., Li, J., Hu, L., & Zheng, X. (2011). Enhanced removal of nitrate by a novel composite: Nanoscale zero valent iron supported on pillared clay. *Chemical Engineering Journal, 171*(2), 526–531. https://doi.org/10.1016/j.cej.2011.04.022

Zhu, Y., Iroh, J. O., Rajagopolan, R., Aykanat, A., & Vaia, R. (2022). Optimizing the synthesis and thermal properties of conducting polymer–montmorillonite clay nanocomposites. *Energies, 15*(4), 1291. https://doi.org/10.3390/en15041291